Measurement of the Nucleon Structure Function F_2 in the Nuclear Medium and Evaluation of its Moments

M. Osipenko[q,af,*], G. Ricco[q], S. Simula[ae], M. Ripani[q], M. Taiuti[q], K.P. Adhikari[aa],
M.J. Amaryan[aa], M. Anghinolfi[q], H. Avakian[ah,p], H. Baghdasaryan[al], M. Battaglieri[q],
V. Batourine[ah], I. Bedlinskiy[t], A.S. Biselli[k,ab], D. Branford[j], W.J. Briscoe[n],
W.K. Brooks[aj,ah], V.D. Burkert[ah], S.L. Careccia[aa], D.S. Carman[ah], P.L. Cole[o,ah],
P. Collins[b,1], V. Crede[m], A. D'Angelo[r,ad], A. Daniel[z], N. Dashyan[an], R. De Vita[q],
E. De Sanctis[p], A. Deur[ah], B Dey[e], S. Dhamija[l], R. Dickson[e], C. Djalali[ag],
D. Doughty[h,ah], R. Dupre[a], H. Egiyan[x,am], A. El Alaoui[a], P. Eugenio[m], S. Fegan[ak],
T.A. Forest[o,aa], A. Fradi[s], M.Y. Gabrielyan[l], N. Gevorgyan[an], G.P. Gilfoyle[ac],
K.L. Giovanetti[u], W. Gohn[i], R.W. Gothe[ag], K.A. Griffioen[am], L. Guo[ah,2], K. Hafidi[a],
H. Hakobyan[aj,an], C. Hanretty[m], N. Hassall[ak], D. Heddle[h,ah], K. Hicks[z], M. Holtrop[x],
Y. Ilieva[ag], D.G. Ireland[ak], E.L. Isupov[af], S.S. Jawalkar[am], H.S. Jo[s], K. Joo[i,aj],
D. Keller[z], M. Khandaker[y], P. Khetarpal[ab], W. Kim[v], A. Klein[aa], F.J. Klein[f,ah],
V. Kubarovsky[ah], S.E. Kuhn[aa], S.V. Kuleshov[aj,t], V. Kuznetsov[v], K. Livingston[ak],
H.Y. Lu[ag], D. Martinez[o], M. Mayer[aa], J. McAndrew[j], M.E. McCracken[e],
B. McKinnon[ak], C.A. Meyer[e], M. Mirazita[p], V. Mokeev[af,ah], B. Moreno[g], K. Moriya[e],
B. Morrison[b], H. Moutarde[g], E. Munevar[n], P. Nadel-Turonski[f,3], R. Nasseripour[ag,4],
S. Niccolai[s], I. Niculescu[u,n], A.I. Ostrovidov[m], R. Paremuzyan[an], K. Park[ag,v,3],
S. Park[m], E. Pasyuk[b,3], S. Anefalos Pereira[p], S. Pisano[s], O. Pogorelko[t],
S. Pozdniakov[t], J.W. Price[c], S. Procureur[g], Y. Prok[al,5], D. Protopopescu[ak],
B.A. Raue[l,ah], G. Rosner[ak], P. Rossi[p], F. Sabatié[g,aa], M.S. Saini[m], J. Salamanca[o],
C. Salgado[y], P. Saracco[q], R.A. Schumacher[e], H. Seraydaryan[aa], Y.G. Sharabian[ah,an],
E.S. Smith[ah], D. Sober[f], D. Sokhan[j,6], S.S. Stepanyan[v], S. Stepanyan[ah,an], P. Stoler[ab],
S. Strauch[ag], D.J. Tedeschi[ag], S. Tkachenko[aa], M. Ungaro[i], B .Vernarsky[e],
M.F. Vineyard[ai,ac], E. Voutier[w], D.P. Watts[ak,7], D.P. Weygand[ah], M.H. Wood[d],
A. Yegneswaran[ah], J. Zhang[aa], B. Zhao[i,8]

[a] *Argonne National Laboratory, Argonne, Illinois 60441*
[b] *Arizona State University, Tempe, Arizona 85287-1504*
[c] *California State University, Dominguez Hills, Carson, CA 90747*
[d] *Canisius College, Buffalo, NY*
[e] *Carnegie Mellon University, Pittsburgh, Pennsylvania 15213*
[f] *Catholic University of America, Washington, D.C. 20064*
[g] *CEA, Centre de Saclay, Irfu/Service de Physique Nucléaire, 91191 Gif-sur-Yvette, France*
[h] *Christopher Newport University, Newport News, Virginia 23606*
[i] *University of Connecticut, Storrs, Connecticut 06269*
[j] *Edinburgh University, Edinburgh EH9 3JZ, United Kingdom*
[k] *Fairfield University, Fairfield CT 06824*
[l] *Florida International University, Miami, Florida 33199*
[m] *Florida State University, Tallahassee, Florida 32306*
[n] *The George Washington University, Washington, DC 20052*
[o] *Idaho State University, Pocatello, Idaho 83209*
[p] *INFN, Laboratori Nazionali di Frascati, 00044 Frascati, Italy*
[q] *INFN, Sezione di Genova, 16146 Genova, Italy*
[r] *INFN, Sezione di Roma Tor Vergata, 00133 Rome, Italy*
[s] *Institut de Physique Nucléaire ORSAY, Orsay, France*
[t] *Institute of Theoretical and Experimental Physics, Moscow, 117259, Russia*
[u] *James Madison University, Harrisonburg, Virginia 22807*

1

^{v}Kyungpook National University, Daegu 702-701, Republic of Korea
^{w}LPSC, Universite Joseph Fourier, CNRS/IN2P3, INPG, Grenoble, France
^{x}University of New Hampshire, Durham, New Hampshire 03824-3568
^{y}Norfolk State University, Norfolk, Virginia 23504
^{z}Ohio University, Athens, Ohio 45701
^{aa}Old Dominion University, Norfolk, Virginia 23529
^{ab}Rensselaer Polytechnic Institute, Troy, New York 12180-3590
^{ac}University of Richmond, Richmond, Virginia 23173
^{ad}Universita' di Roma Tor Vergata, 00133 Rome, Italy
^{ae}INFN, Sezione di ROMA III, 00146 Rome, Italy
^{af}Skobeltsyn Nuclear Physics Institute, Skobeltsyn Nuclear Physics Institute, 119899 Moscow, Russia
^{ag}University of South Carolina, Columbia, South Carolina 29208
^{ah}Thomas Jefferson National Accelerator Facility, Newport News, Virginia 23606
^{ai}Union College, Schenectady, NY 12308
^{aj}Universidad Técnica Federico Santa María, Casilla 110-V Valparaíso, Chile
^{ak}University of Glasgow, Glasgow G12 8QQ, United Kingdom
^{al}University of Virginia, Charlottesville, Virginia 22901
^{am}College of William and Mary, Williamsburg, Virginia 23187-8795
^{an}Yerevan Physics Institute, 375036 Yerevan, Armenia

Abstract

We report on the measurement of inclusive electron scattering off a carbon target performed with CLAS at Jefferson Laboratory. A combination of three different beam energies 1.161, 2.261 and 4.461 GeV allowed us to reach an invariant mass of the final-state hadronic system $W \approx 2.4$ GeV with four-momentum transfers Q^2 ranging from 0.2 to 5 $(GeV/c)^2$. These data, together with previous measurements of the inclusive electron scattering off proton and deuteron, which cover a similar continuous two-dimensional region of Q^2 and Bjorken variable x, permit the study of nuclear modifications of the nucleon structure. By using these, as well as other world data, we evaluated the F_2 structure function and its moments. Using an OPE-based twist expansion, we studied the Q^2-evolution of the moments, obtaining a separation of the leading-twist and the total higher-twist terms. The carbon-to-deuteron ratio of the leading-twist contributions to the F_2 moments exhibits the well known EMC effect, compatible with that discovered previously in x-space. The total higher-twist term in the carbon nucleus appears, although with large systematic uncertainties, to be smaller with respect to the deuteron case for $n < 7$, suggesting partial parton deconfinement in nuclear matter. We speculate that the spatial extension of the nucleon is changed when it is immersed in the nuclear medium.

Keywords: moments, nuclear modifications, nucleon structure, higher twists, QCD, OPE
PACS: 12.38.Cy, 12.38.Lg, 12.38.Qk, 13.60.Hb

1. Introduction

Inclusive electron scattering off a nucleus, $e(k)+A(P) \rightarrow e'(k')+X$, may be expressed, under the one photon exchange approximation, in terms of the total absorption of a virtual photon by the nucleus: $\gamma^*(q = k - k') + A(P) \rightarrow X$. At sufficiently large squared four-momentum transfer, $Q^2 = -q^2$, the coherent electron-nucleus scattering contribution is negligible, facilitating a description of the scattering in terms of individual nucleons in the nuclear matter. The inclusive electron-nucleon scattering cross section is related to the parton momentum distribution along the virtual photon (longitudinal) direction. This structure, however, depends on the environment in which the nucleon is embedded. In particular, the nuclear medium environment interferes with the nucleon internal structure. The experimental evidence for such nuclear modifications in the Deep Inelastic Scattering (DIS) regime was found by the European Muon Collaboration (EMC) [1]. Other similar observations came from intermediate energy experiments that observed changes in the nucleon and nucleon excited state form-factors [2]. In order to study the transition of the nuclear modifications from the DIS regime (EMC effect) to the larger spacial scale region (the nucleon and its excited state form-factors), the structure function F_2 is calculated from the cross section and used to perform a Mellin transform to moments M^{CN}. The Mellin transform allows to express the observable from Minkowski x-space (x-representation of $F_2(x)$) in Euclidean space of moments (n-representation of M_n^{CN}), where Lattice QCD method works.

The Cornwall-Norton moments M_n^{CN} of the nucleon (in the nucleus with mass M_A) structure functions are defined as:

$$M_n^{CN}(Q^2) = \int_0^{M_A/M} dx x^{(n-2)} F_2(x, Q^2), \quad n \geq 2, \, n \text{ even}, \qquad (1)$$

where M is the nucleon mass, $x = -Aq^2/2Pq$ is the Bjorken variable per nucleon and n is the order of the moment. Quantum Chromodynamics (QCD) predicts the Q^2-evolution of these moments for each given n [3]. Moreover, the DIS component of these moments and the contribution of the nucleon and the nucleon excited state form-factors have different Q^2 behaviors [4]. Therefore, the study of the Q^2 dependence of the structure function moments is important for understanding the nucleon modifications in the nuclear medium.

The identification of these nuclear modifications to the nucleon structure in inclusive electron scattering is complicated by the presence of other nuclear effects [5]. The most important effect comes from the motion of the nucleon in the nucleus, known as Fermi motion. There are also other effects that cannot be reduced to the total absorption of the virtual photon by the nucleon. These are shadowing, Final State Interactions (FSIs)

*Corresponding author: osipenko@ge.infn.it
[1] Current address: Washington, D.C. 20064
[2] Current address: New Mexico, NM
[3] Current address: Newport News, Virginia 23606
[4] Current address: Washington, DC 20052
[5] Current address: Newport News, Virginia 23606
[6] Current address: Orsay, France
[7] Current address: Edinburgh EH9 3JZ, United Kingdom
[8] Current address: Williamsburg, Virginia 23187-8795
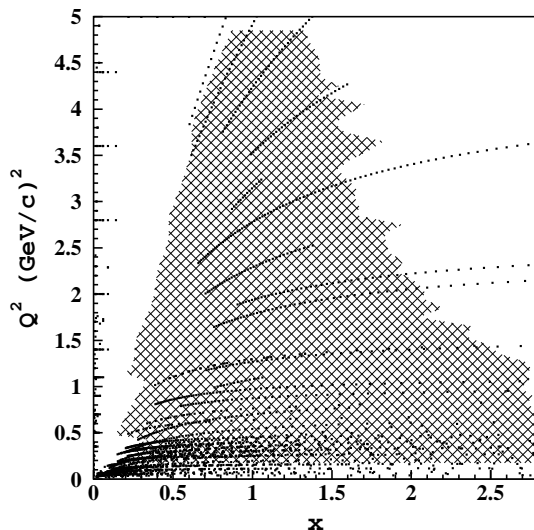
Figure 1: Experimental data on the carbon structure function $F_2(x, Q^2)$ used for the moment evaluation in the CLAS kinematic region. The points show the world data from Refs. [10, 11, 12, 13, 14, 15, 16, 17, 18, 19, 20, 21, 22, 23, 24, 25, 26, 27, 28, 29, 30, 31, 32, 33, 34, 35]. The shaded area shows the CLAS data region.

and Meson Exchange Currents (MECs). However, the latter ones are typically smaller and can be localized by their kinematic regions of influence.

The study of nuclear modifications can be performed by comparing the nucleon structure of a free nucleon to one bound in the nuclear medium. To this end, the proton and deuteron structure function moments were previously measured in Refs. [6, 7]. The present article maintains the same framework of these two previous measurements in order to avoid additional bias due to the analysis technique.

Similar studies were performed in the past in Ref. [8] and recently repeated by the Hall C Collaboration at Jefferson Lab [9], and reported contradictory results. In this paper, we increase the precision of the previous studies by a new measurement of unpolarized inclusive electron scattering on carbon, performed with the CLAS detector in Hall B at Jefferson Lab. Like in the case of the proton and deuteron measurements, the new data cover a wide continuous two-dimensional region in x and Q^2 as shown in Fig. 1.

In Section 2 we describe the QCD picture of the F_2 moments. In Section 3 we discuss some data analysis details. For further information we refer to Refs. [6, 7], from which many procedures are adopted. Finally, in Sections 4 and 5 we present our main results.

2. QCD Analysis of Nucleon Structure

QCD-based descriptions of inclusive lepton scattering can require Operator Product Expansion (OPE) machinery [3]. The OPE expresses the structure function moments in

4

a power series:

$$M_n^{CN}(Q^2) = \sum_{\tau=2k}^{\infty} E_{n\tau}(\mu_r, \mu_f, \alpha_S) O_{n\tau}(\mu_f) \left(\frac{\mu^2}{Q^2}\right)^{\frac{1}{2}(\tau-2)},$$ (2)

where $k = 1, 2, ..., \infty$, μ_f (μ_r) is the factorization (renormalization) scale[1] and μ is an arbitrary reference scale. $O_{n\tau}(\mu_f)$ is the reduced matrix element of the local operators with definite spin n and twist τ (dimension minus spin). This quantity is related to the partonic structure of the target. $E_{n\tau}(\mu_r, \mu_f, \alpha_S)$ is a dimensionless coefficient function. For sufficiently large Q^2 and therefore small running coupling constant $\alpha_s(Q^2)$, it can be analytically calculated in perturbative QCD (pQCD).

The first term in this expansion (the leading twist):

$$\eta_n(Q^2) = E_{n2}(\mu_r, \mu_f, \alpha_S) O_{n2}(\mu_f),$$ (3)

can be completely evaluated in QCD. The operator matrix elements O_{n2}, given by the expectation values of the parton momentum distributions in the nucleon, are calculated in Lattice QCD [37] for $n = 2, 4$. The coefficient functions are calculated in pQCD [38] at α_S^2 precision, including resummation of specific effects in the large-x region to $\ln^2(\alpha_S)$ precision [36, 39]. This term is responsible for the DIS inclusive cross section and its modification in nuclei gives rise to the EMC effect.

Further terms are far less known, but can be studied phenomenologically by exploiting the general form of their Q^2-dependence. The separation of individual twists related to specific QCD operators is not possible without knowledge of the corresponding coefficient functions, but the total higher-twist term:

$$HT_n(Q^2) = \frac{\mu^2}{Q^2} \sum_{\tau=4}^{\infty} E_{n\tau}(\mu_r, \mu_f, \alpha_S) O_{n\tau}(\mu_f) \left(\frac{\mu^2}{Q^2}\right)^{\frac{1}{2}(\tau-4)}$$ (4)

contribution can still be analyzed. This total higher-twist term is responsible for the multi-parton correlations in the nucleon and, therefore, it is connected also to the nucleon elastic form-factors and to the transition form-factors to the nucleon excited states. If there are nucleon modifications of these properties that are important at lower Q^2, higher twists can be used to investigate them.

In summary, a comparison of the leading-twist moments of the nucleon structure function in complex nuclei to that in the deuteron allows a study of the EMC effect in the moment space $(M_n(Q^2))$. This allows a direct comparison to Lattice QCD calculations of the nucleon modified by the presence of the medium. A similar comparison between the total higher-twist moments in deuteron and nuclei allows study of the nuclear modifications of confinement and multi-parton correlations.

3. Data Analysis

The data were collected at Jefferson Lab in Hall B with the CEBAF Large Acceptance Spectrometer (CLAS) using a solid, 0.18 g/cm^2 thick, carbon target during the electron

---

[1]We are working in the Soft Gluon Re-summation (SGR) scheme [36], where $\mu_f^2 = \mu_r^2 = Q^2$.

beam running period in April-May 1999. The average luminosity was 6×10^{33} cm^{-2}s^{-1}. Data were recorded using electron beam energies $E_0 = 1.161$, 2.261 and 4.461 GeV to maximize the Q^2 and x kinematics range. The accumulated statistics at the three energies allows a measurement of the inclusive cross section with a statistical uncertainty ($\leq 5\%$) in x and Q^2 intervals of $\Delta x = 0.009$ and $\Delta Q^2 = 0.05\text{-}0.1$ (GeV/c)^2.

CLAS is a magnetic spectrometer [40] based on a six-coil torus magnet whose field is primarily oriented along the azimuthal direction. The sectors, located between the magnet coils, are individually instrumented to form six independent magnetic spectrometers. The particle detection system includes Drift Chambers (DC) for track reconstruction [41], Scintillation Counters (SC) for time-of-flight measurements [42], Cherenkov Counters (CC) for electron identification [43], and Electromagnetic Calorimeters (EC) to measure neutrals and to improve electron-pion separation [44]. The EC detectors, which have a granularity defined by triangular cells in a plane perpendicular to the incoming particles, are used to study the shape of the electromagnetic shower and are longitudinally divided into two parts with the inner part acting as a pre-shower.

Charged particles can be detected and identified for momenta down to 0.2 (GeV/c) and for polar angles between 8° and 142°. The CLAS superconducting coils limit the acceptance for charged hadrons from about 80% at $\theta = 90°$ to about 50% at forward angles ($\theta = 20°$). The total angular acceptance for electrons is about 1.5 sr. Electron momentum resolution is a function of the scattered electron angle and varies from 0.5% for $\theta \leq 30°$ up to 1-2% for $\theta > 30°$. The angular resolution is approximately constant, approaching 1 mrad for polar and 4 mrad for azimuthal angles: the resolution for the momentum transfer ranges therefore from 0.2 up to 0.5 %. The scattered electron missing mass (W) resolution was estimated to be 2.5 MeV for a beam energy less than 3 GeV and about 7 MeV for larger energies. To study all possible multi-particle states, the acquisition trigger was configured to require at least one electron candidate in any of the sectors, where an electron candidate was defined as the coincidence of a signal in the EC and Cherenkov modules for any one of the sectors.

The data analysis procedure has been described in detail in Refs. [6, 7]. Therefore, in this article we focus on changes and improvements in the analysis. The most important improvements, leading to a significant reduction of the estimated systematic uncertainties relative to those of Refs. [6, 7], are described in the following sections.

3.1. Generic Procedures

Phenomenological corrections to the reconstructed charged particle momentum were applied to compensate for small drift chamber misalignments and torus magnetic field map inaccuracies. These corrections were determined by subtracting the missing mass spectrum (W) measured using a solid carbon target from a measurement using CH$_2$ in order to extract the proton elastic scattering response. The scattered electron momentum measurement was shifted for the entire W spectrum in such a way that the elastic scattering peak was at the correct position of $W = 938$ MeV/c^2. This was accomplished by making a fit of the hydrogen elastic peak distributions for a few azimuthal angle bins inside each sector under the assumption that the polar angle was measured precisely. These corrections were applied for each sector separately and improved the elastic missing mass resolution by 15%. For the highest beam energy data set, the statistics from hydrogen were insufficient to determine momentum corrections. However, the Fermi motion at these Q^2 values leads to a very smooth cross section having no peaks or other
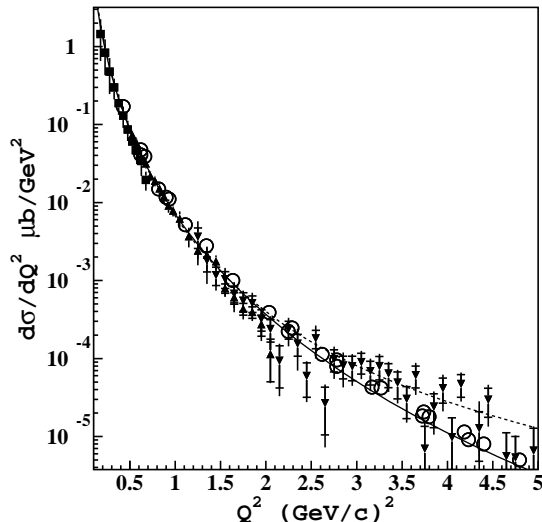
Figure 2: Hydrogen elastic scattering cross section extracted by means of CH_2-C subtraction for three different beam energies: full squares - 1.161 GeV, full triangles - 2.261 GeV, reversed full triangles - 4.461 GeV. The inner error bars show statistical uncertainties, while the outer error bars represent the statistical and systematic uncertainties summed in quadrature. The cross sections are compared with the data from Ref. [45] (empty circles) and with parametrization based on dipole form-factors (dashed line) including also radiative corrections (solid line).

structures and, therefore, makes it relatively insensitive to possible small systematic uncertainties in the measured momentum. To check the absolute normalization of our data we subtracted the carbon data from CH_2 yield and obtained the cross section of the scattering on hydrogen. The elastic scattering cross section was selected and compared to the previous data from Ref. [45] and to the dipole parametrization. The comparison, shown in Fig. 2, exhibits fairly good agreement, although with large systematic uncertainties, related to the small fraction of hydrogen events in the total CH_2 yield.

Although the results of the present analysis use realistic Monte Carlo simulations of the CLAS detector, such simulations have limited reliability at the edges of the detector's sensitive volume. There are also small regions of the CLAS detector that were very inefficient and, in some cases, were malfunctioning. These regions were eliminated using kinematic cuts to simplify the analysis. The kinematic cuts were defined as functions of the measured scattered electron momentum and angle to establish fiducial volumes with a uniform detector efficiency in the polar angle ϕ. These cuts along the edges of the acceptance removed about 50% of the recorded data.

3.2. Electron Identification

Electrons were identified in CLAS by a coincidence between signals from the Electromagnetic Calorimeter (EC) and the Cherenkov Counter (CC). Furthermore, only events with a reconstructed Drift Chamber (DC) negatively charged particle track that matches these hits were selected.

7

The CLAS Cherenkov Counter (CC) inefficiency does not exceed 2% within the fiducial regions of the CLAS acceptance [6, 7]. However, the electron-pion separation does not work at the same level of precision and some pion contamination shows up in the electron candidate sample. This is especially important at high beam energies (e.g. for the 4.461 GeV data set), where the number of low momentum pions is significant.

The pion contamination in the electron candidate sample appears as a single photo-electron peak in the measured CC spectra (see Fig. 3). The main source of this contamination is the result of an accidental coincidence between a pion produced by quasi-real photoproduction with random noise in one of the 36 CC PMTs. This coincidence takes place due to the loose matching between the CC hit and the track within one sector of CLAS. A procedure was developed in Ref. [46] to geometrically and temporally match a CC hit with a track seen in the DC and a hit in the SC. The resulting Cherenkov distribution is shown in Fig. 3. The reconstruction algorithm eliminated the pion contamination in the single-photoelectron peak, which in the worst case could reach 20%.

The Electromagnetic Calorimeter (EC) is used to separate pions from electron candidates with momenta above the pion threshold (2.7 GeV/c). Electrons entering in the EC release $\sim 30\%$ of their energy in the sensitive volume on average, while pion losses are constant (see Fig. 4). This EC property was exploited at large particle momenta for electron-pion separation by selecting particles with an energy fraction released in the EC above 20%. More details on this procedure can be found in Ref. [6]. Furthermore, pions just above the Cherenkov threshold produce less Cherenkov light with respect to electrons of the same momenta and, therefore, can be removed by a cut on the number of photoelectrons measured in the CC.
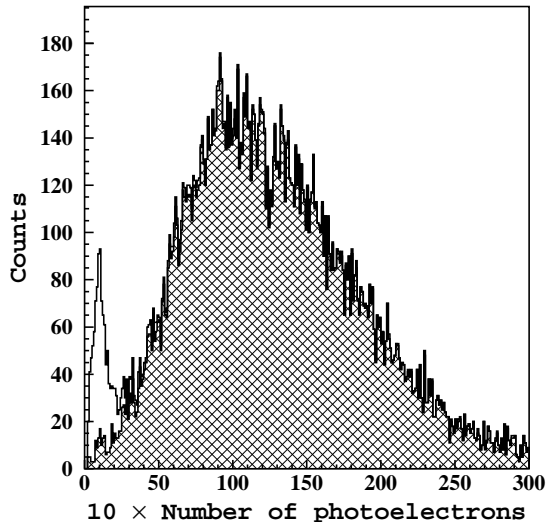
Figure 3: The spectrum of photoelectrons measured in one sector of the CC at $\nu = 3.4$ GeV (beam energy 4.461 GeV). The hatched area represents the CC spectrum after applying the matching procedure described in the text.
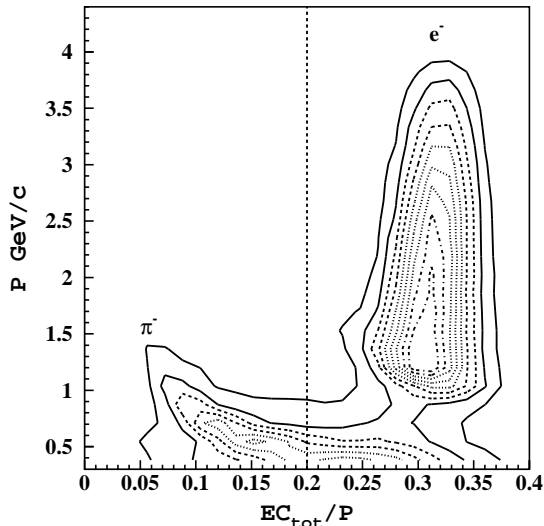
Figure 4: Electron-pion separation in the Electromagnetic Calorimeter (EC) of CLAS: the left peak at small released energy fraction is due to pions and the right peak at $EC_{tot}/\mathbf{P} \sim 0.3$ represents the electron signal. The dashed line shows the cut applied to the data.

3.3. Background

The creation of e^+e^- pairs by real photons or through hadronic decays and the scattering of electrons from materials other than the target are the dominant sources of background electrons.

3.3.1. e^+e^- pair production

The main source of e^+e^- pairs entering the CLAS acceptance is from π^0 production, followed by either Dalitz decay to γe^+e^- or π^0 decay to $\gamma\gamma$, where one of the photons converts to an e^+e^- pair. A model using a Wiser fit to inclusive pion photoproduction was used to effectively reproduce the positron cross sections observed in a previous CLAS experiment [47]. The above model was used to estimate the e^+e^- contribution to the measured inclusive cross section. The value of the contribution was assumed to be equal to the ratio of the inclusive e^+ production cross section over the inclusive nuclear scattering parametrization [8, 48] including radiative processes (tail from elastic peak, bremsstrahlung and Schwinger correction):

$$F_{e^+e^-}(E_0, x, Q^2) = \frac{\sigma^M_{rad}(E_0, x, Q^2)}{\sigma^M_{rad}(E_0, x, Q^2) + \sigma_{e^+}(E_0, x, Q^2)} \quad , \tag{5}$$

where σ_{e^+} is the inclusive e^+ production cross section, equal to the integral of the π^0 quasi-real electroproduction cross section folded with its decay probability and integrated over the allowed kinematic range, and σ^M_{rad} is the inclusive nuclear scattering parametrization [8, 48] folded with radiative processes, as described in Ref. [6].

In this parametrization the π^0 quasi-real electroproduction cross section is given by:

$$\frac{d\sigma_{ep\to hX}}{dp_h d\Omega_h} = \frac{P_h^2}{E_h}\int_{E_\gamma^{min}}^{E_0}\frac{dE_\gamma}{E_\gamma}\left\{\frac{t_{ext}}{2}+t_{int}\right\}E_h\frac{d^3\sigma_{\gamma p\to hX}}{d^3 p_h}\left[e^{C_1 M_L}e^{C_2 p_T^2/E_h}\right] \ , \qquad (6)$$

where $\sigma_{\gamma p\to hX}$ is the parametrized photoproduction cross section, P_h and E_h are the pion momentum and energy, p_T is the pion transverse momentum with respect to the photon direction, E_0 is the electron beam energy, E_γ is the exchanged photon energy, t_{int} and t_{ext} are the internal and external radiator thicknesses and $M_L = \sqrt{p_T^2 - m_h^2}$, with m_h being the pion mass. C_1 and C_2 are the Wiser fit parameters.

The external radiator thickness is small compared to the second term, $t_{ext} = 0.0053$ radiation lengths. The internal radiator length used to estimate the e^+ rate (previously assumed to be 5%) was evaluated according to the Weizsacker-Williams formula [49]:

$$t_{int} = \frac{\alpha}{2}\left[\frac{E_0^2 + E'^2}{E_0^2}\left(\log\frac{E_0}{m_e}-\frac{1}{2}\right)+\frac{E_\gamma^2}{2E_0^2}\left(\log\frac{2E'}{E_\gamma}+1\right)+\frac{(E_0+E')^2}{2E_0^2}\log\frac{2E'}{E_0+E'}\right] \ , \ (7)$$

where E' is the scattered electron energy and m_e is the electron mass.

The largest $e^+ e^-$ contribution is less than 9% of the inclusive cross section at x of 0.2 as shown in Fig. 5 and only impacts the data taken at 2.261 and 4.461 GeV beam energies, where such low values of x are accessible.
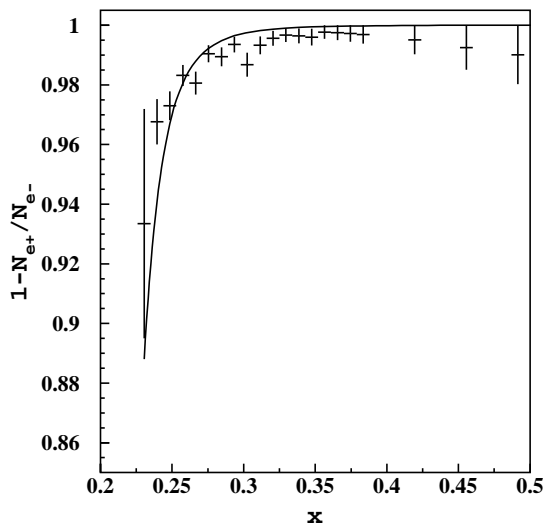
Figure 5: The contribution of $e^+ e^-$ pair production events in the inclusive cross section at $Q^2 = 1.55$ (GeV/c)^2. The numbers of positrons N_{e+} and electrons N_{e-} were obtained from different runs with opposite CLAS torus magnetic fields, allowing for a cancellation of the acceptance and efficiency in the ratio. The points show the measured quantity $1 - N_{e+}/N_{e-}$, which represents the ratio of the number of electrons inelastically scattered off carbon to the total number of measured electrons. The curve represents the calculations from Eq. 5.

3.3.2. Target Cell Contribution

The target wall contribution to the measured cross section has been removed using empty target data in bins of the energy E_0, the Bjorken scaling variable x and Q^2 such that:

$$N_C(E_0, x, Q^2) = N_{full}(E_0, x, Q^2) - \frac{Q_{tot}^{full}}{Q_{tot}^{empty}} N_{empty}(E_0, x, Q^2) \quad , \tag{8}$$

where N_{full}, N_{empty} and N_C are the number of events in the full target data, the empty target data and the number of events due to scattering off the carbon target, respectively. Q_{tot}^{full} and Q_{tot}^{empty} represent the charge accumulated in full and empty target runs as measured by a Faraday Cup (FC) gated by the data acquisition live time. Any inaccuracy of the Z-vertex reconstruction (see Fig. 6) did not affect the extracted cross section because this information was not used in the evaluation procedure.

Multiple scattering and elastic electron-nucleus scattering at the lowest beam energy of $E_0 = 1.161$ GeV caused the incident electron beam to diverge after passing through a full target such that a small fraction of the beam was no longer within the FC acceptance. This resulted in charge loss. A precise experimental determination of the charge loss was performed using the measured cross section of electron scattering by the empty target walls (Mylar/Aluminum windows of the empty cell for liquids). Electrons scattered by the empty cell walls were selected according to their reconstructed Z-vertex shown in Fig. 6. The evident enhancement of the full target data is due to the FC charge loss. The overall normalization factor was estimated by selecting the region of Z from -6 cm to 3 cm in both empty and full target data and evaluating the ratio:

$$F_{norm} = \frac{\int_{z=-6cm}^{z=3cm} \sigma_{tot}^{full} dz}{\int_{z=-6cm}^{z=3cm} \sigma_{tot}^{empty} dz} \quad , \tag{9}$$

where $\sigma_{tot}^{full,empty}(Z) = \frac{1}{\rho \frac{N_A}{M_A} L Q_{tot}} N_{events}^{full,empty}(Z)$ is the total cross section for the target corresponding to a given Z interval (for definition of variables see Section 3.5). The correction factor was found to be $F_{norm}^{1.161GeV} = 1.1459$ with negligible statistical uncertainty. Selecting only the first empty target cell window using the cut on Z from -6 cm to -1 cm gives the same ratio within 0.2%. The corresponding Z-vertex distribution shows good agreement between the empty and full target cross sections using the above correction factor F_{norm}. Numerical estimates for $E_0 = 4.461$ GeV data give the ratio $F_{norm}^{4.461GeV} = 1.0006 \pm 0.006$ for the Z-cut from -10 cm to -2.5 cm. A systematic uncertainty of 3% was assigned to the FC charge loss correction for the $E_0 = 1.161$ GeV data set based on the above analysis.

3.4. Acceptance and Efficiency Evaluation

Determination of the acceptance and efficiency corrections was based entirely on the Monte Carlo (MC) simulations developed for CLAS. Moreover, the systematic uncertainties of these corrections were estimated from a comparison of MC simulations with experimental data using a realistic model in the event generator. In short, the procedure was the following: we generated events with the event generator describing elastic, quasi-elastic and inelastic eC-scattering processes including radiative corrections. These events then were processed with the GEANT-based CLAS software simulating the detector response. After that the standard CLAS event reconstruction procedure was applied.

11
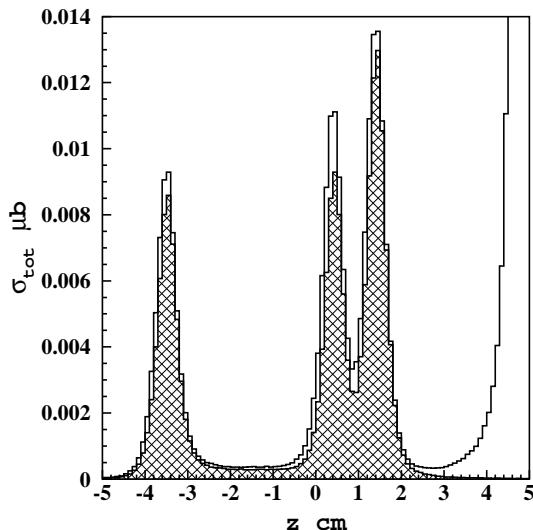
Figure 6: Z-vertex distribution for the carbon target in (open histogram), and carbon target out (hatched histogram) at $E_0 = 1.161$ GeV. The large peak that can be partially seen on the right side of the plot is due to scattering off the carbon plate, while the three smaller peaks are due to the empty target windows.

Finally, the ratio of reconstructed events to the number of generated events gave a combined efficiency/acceptance correction in each kinematic bin.

Detector response simulations were performed in the same way as described in Ref. [6]. The following improvements and changes for electron-nucleus scattering were implemented:

1. Electron scattering events were generated by a random event generator with the probability distributed according to σ_{rad}^{M}. The values for the elastic and inelastic cross sections for electron-carbon scattering were taken from existing fits of world data in Refs. [50] and [8, 48], respectively.

2. The contribution from internal radiative processes was added according to calculations [51].

3. The event rate obtained in the simulations was then compared to the data, preserving the original normalizations (accumulated FC charge for the data and the number of generated events over the integrated cross section of the event generator for simulations). These normalized yields differ from the cross section by the acceptance, efficiency and radiative corrections. The simulated events were subjected to the same cuts applied to the data. e^+e^- pair production and empty target backgrounds were subtracted from the data. The normalized yields obtained with the same set of cuts from the data and simulations were compared and found to be in good agreement at $x < 1.5$ (see Fig. 7). At larger x, the contribution of nucleon short range correlations (SRC), which are not included in the model, may play a significant role [52, 53].

The efficiency appears to be fairly flat and not lower than 97% inside the region of the detector defined by the fiducial cuts.

12
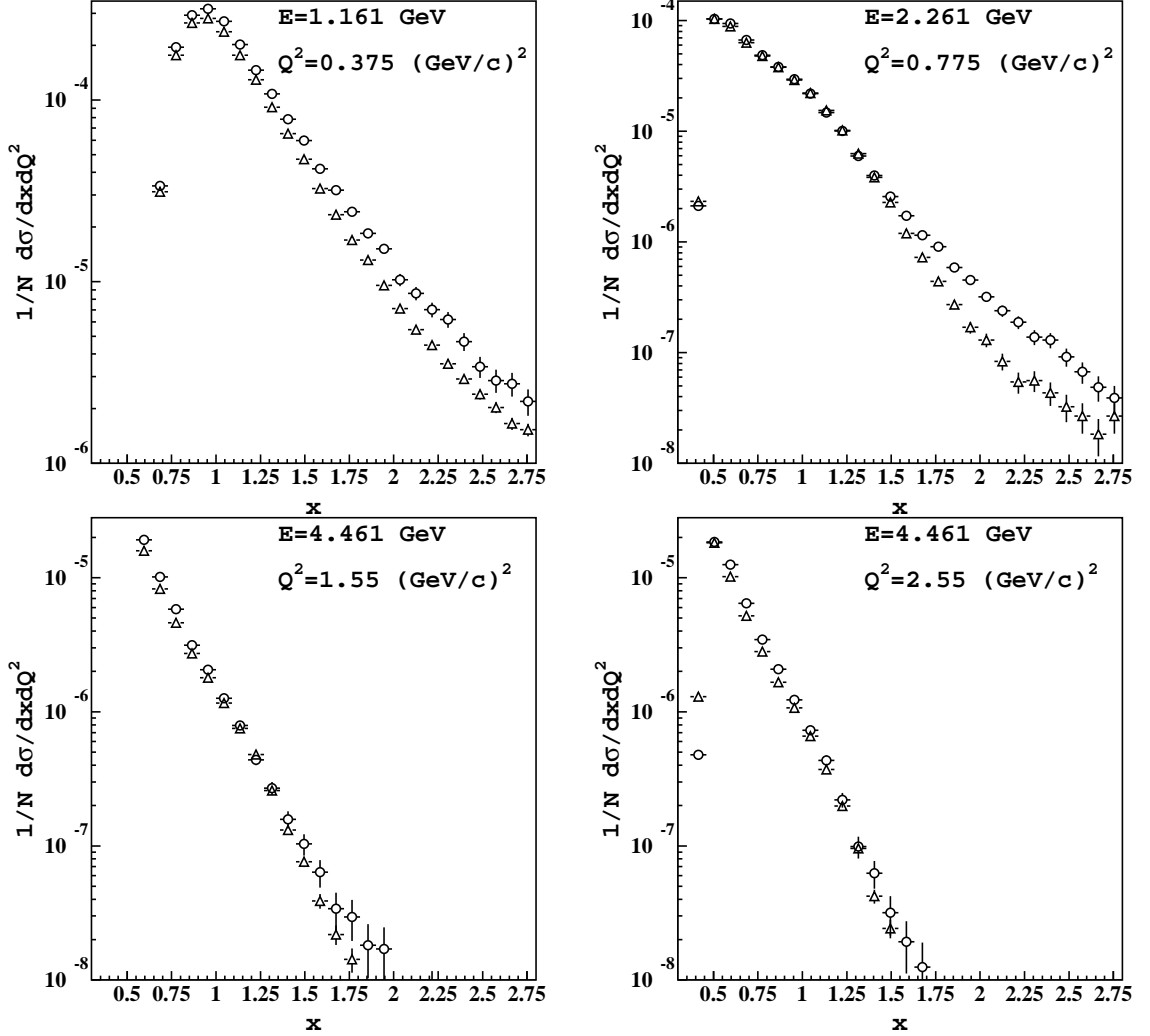
Figure 7: Comparison of normalized yields from the data (open circles) and reconstructed Monte Carlo (open triangles) for four different kinematic settings. The error bars include only statistical uncertainties.

3.5. Structure Function $F_2(x, Q^2)$

The measured electron yield N_C, normalized to the integrated luminosity in conjunction with Monte Carlo simulations, were used to extract the structure function F_2 in each kinematic bin. The Monte Carlo events were used to simultaneously obtain efficiency, acceptance, bin centering and radiative corrections. F_2 has been determined using:

$$F_2(x, Q^2) = \frac{1}{\rho \frac{N_A}{M_A} A L Q_{tot}} \frac{J}{\sigma_{Mott}} \frac{\nu}{1 + \frac{1-\epsilon}{\epsilon} \frac{1}{1+R}} \frac{N_C(x, Q^2)}{\Psi(x, Q^2)} F_{e^+ e^-}(x, Q^2) , \qquad (10)$$

13

where $\nu = E_0 - E'$ is the energy transfer, ρ is the density of the carbon target, N_A is the Avogadro constant, M_A is the target molar mass, L is the target length, Q_{tot} is the total charge in the Faraday Cup (FC) and $\Psi(x, Q^2)$ is the efficiency including the radiative and bin-centering correction factors:

$$\Psi(x, Q^2) = \Psi_{eff}(x, Q^2)\Psi_{rad}(x, Q^2)\Psi_{bin}(x, Q^2) , \tag{11}$$

with:

$$\Psi_{rad} = \frac{\sigma_{rad}^M}{\sigma^M} \quad \text{and} \quad \Psi_{bin} = \frac{\int_{\Delta\tau} d\sigma^M}{\sigma^M} . \tag{12}$$

Ψ_{eff} is the ratio between the number of reconstructed and generated events in the bin and σ^M is the event generator model cross section. The integral in Eq. 12 was taken over the bin area $\Delta\tau$. Here ϵ is the virtual photon polarization parameter:

$$\epsilon \equiv \left(1 + 2\frac{\nu^2 + Q^2}{Q^2}\tan^2\frac{\theta}{2}\right)^{-1} . \tag{13}$$

The Mott cross section σ_{Mott} and the Jacobian J of the transformation between $d\Omega dE'$ to $dx dQ^2$ are defined by:

$$\sigma_{Mott} = \frac{\alpha^2 \cos^2\frac{\theta}{2}}{4E_0^2 \sin^4\frac{\theta}{2}} \quad \text{and} \quad J = \frac{xE_0 E'}{\pi\nu} . \tag{14}$$

The structure function $F_2(x, Q^2)$ was extracted using the fit of the function $R(x, Q^2) \equiv \sigma_L/\sigma_T$ described in Ref. [7]. However, the structure function F_2 in the relevant kinematic range is very insensitive to the value of R. For example, at the typical kinematics of $\epsilon = 0.75$ and assuming a SLAC DIS R value of 0.18, the relative uncertainties of F_2 and R are related by $\Delta F_2/F_2 = 0.03\Delta R/R$. Therefore, at this kinematics a relative error in R of 20% will generate only a relative error of 0.6% in F_2. The overlapped data from two different beam energies were combined using a weighted-average technique. Moreover, we checked that the parametrization used for R was consistent with the difference between the two cross sections within statistical and systematic uncertainties.

Fig. 8 shows a comparison between the F_2 data from CLAS and the other world data in a few Q^2 bins. The CLAS data agree very well with all previous measurements. The measured $F_2(x, Q^2)$ values are given in the center of the corresponding x and Q^2 bin. The Monte Carlo based bin centering correction from Eq. 12 allows to interpolate the data averaged over the bin to its value in the middle of the bin. Therefore, we do not provide any uncertainty in the determination of x and Q^2. However, this uncertainty is implicitly included in the systematic uncertainties of Monte Carlo simulations. Indeed, Monte Carlo simulations include the effect of event migration from the original bin to neighbor bins, due to the finite detector resolution and energy loss in the target. Hence, the loss or gain of events in each single bin in the data is compensated by a similar change of the number of Monte Carlo events. As a test, we verified that the data obtained within significantly larger, not rectangular bins (in which bin migration is suppressed) agree with the presented data within statistical uncertainties. The values of $F_2(x, Q^2)$, together with their statistical and systematic uncertainties, are tabulated elsewhere [54].

The radiative correction factor Ψ_{rad} was calculated in the following way:

14

- the eC elastic radiative tail was calculated according to the "exact" Mo and Tsai formula [51];

- in the quasi-elastic peak region ($W^{el} + \Delta W < W < 1.2$ GeV) we have applied the correction formula to the continuum spectrum given in Ref. [51], which is based on the peaking approximation and is known to be reliable only when $E'/E_0 > 0.5$. Here W^{el} is the eC elastic peak position and ΔW is its width;

- at $W > 1.2$ GeV we applied the exact Mo and Tsai formula to the quasi-elastic tail, while a formula based on the peaking approximation (referred to as the "unfolding procedure") was used for the inelastic spectrum. For an exact calculation of the quasi-elastic tail, it was necessary to extract quasi-elastic form-factors. To this end we integrated the quasi-elastic cross section given by our parametrization from the beginning of the peak up to $W = 1.2$ GeV and performed a separation of the electric and magnetic form-factors. The tails calculated in these two kinematic regions do not exhibit any discontinuity at the point $W = 1.2$ GeV. This assured us that the peaking approximation formalism is safely applicable to the quasi-elastic tail up to $W = 1.2$ GeV.

The radiative correction factor Ψ_{rad} varies strongly in the explored kinematic range from 0.7 up to 1.5. Fortunately, the largest corrections are given by the tails of the elastic and quasi-elastic peaks, for which calculations are very accurate (of the order of percent, see Refs. [51, 55]).

3.6. Systematic Uncertainties

Here we summarize all the systematic uncertainties taken into account in the present analysis:

- The cross section overall normalization carries a systematic uncertainty due to the known precision of the target length and thickness. We estimated this uncertainty to be 1%. For the lowest beam energy set, $E_0 = 1.161$ GeV, an additional systematic uncertainty due to FC charge loss corrections of 3% was added.

- Previous CLAS inclusive measurements [6, 7] on proton and deuteron targets showed that the combined efficiency/acceptance systematic uncertainty of CLAS data averaged to 4.5%. We assumed a 3% uniform systematic uncertainty due to the efficiency evaluation, while the systematic uncertainty on the acceptance, based on Monte Carlo simulations, was evaluated separately.

- There are two systematic uncertainties in the Monte Carlo simulation. The first one is due to the model dependence of the reaction cross section used for generating the events. Taking into account the good agreement between the data and Monte Carlo simulations we neglected this uncertainty. The second systematic uncertainty is due to the inability of the GEANT3-based CLAS simulation package GSIM [56] to reproduce the CLAS response to electron tracks at different angles and momenta. To estimate this effect, we treated the six CLAS sectors as independent spectrometers. The normalized event yield measured in each sector was compared separately to the simulations, as shown in Fig. 7. The observed differences were compared sector-by-sector to remove uncertainties due to the event generator model. From

15

this comparison, we obtained an average systematic uncertainty varying for different data sets from 5 to 8%.

- The e^+e^--pair production correction introduces a systematic uncertainty due to the parametrization involved in the calculations. We assumed 30% uncertainty on the inclusive e^+ cross section [47] and 10% on the inelastic electron-carbon cross section [8, 48]. The systematic uncertainty is kinematics dependent, but since the correction is very close to unity, the systematic uncertainty associated with it never exceeds 5%.

- e^--identification is based on the CC signal. The correlation of the CC to a particle track is dependent on the magnitude of the CC signal. Therefore, the systematic uncertainty is related to the mean number of photoelectrons in each kinematic point. The inefficiency of the CC signal is given by $[1 - \exp(-N_{phe})]$, where N_{phe} is the mean number of photoelectrons. We took this probability as an estimate of the systematic uncertainty due to e^--identification.

- The systematic uncertainties of the radiative corrections (RC) were estimated by changing the various parametrizations used in the RC evaluation, and computing the differences with the standard parametrization. In particular, we changed the elastic ^{12}C form-factor by 10%, the quasi-elastic cross section by $[10 + 40/(1 + Q^2/M^2)]$ % and the inelastic cross section by 10%. The three obtained differences were combined in quadrature to extract the final systematic uncertainty of the radiative corrections.

- Since we applied corrections to the measured e^- momentum, we estimated the related systematic uncertainty. The momentum correction that brings the hydrogen elastic peak to the correct position results in an average momentum shift of $0.003\Delta p/p$ for $E_0 = 1.161$ GeV and of $0.0035\Delta p/p$ for $E_0 = 2.261$ GeV. For $E_0 = 4.461$ GeV we assumed that the possible momentum shift can be slightly larger than the two measured values for the lower energies, $0.004\Delta p/p$. We shifted the entire data spectra by the abovementioned amounts to evaluate the relative change of the cross section in each bin. This modified relative change gave us an estimate of the uncertainty on the measured cross section. For the two lower beam energies, these relative shifts were suppressed by the factor accounting for the fixed value of the momentum at the hydrogen elastic peak position. This factor, which reduced the uncertainty in the vicinity of the hydrogen elastic peak, was parametrized as $[1 - \exp(-(\nu - Q^2/2M)^2/(2\sigma_p^2))]$, where the width parameter σ_p was taken to be 0.3 GeV for the $E_0 = 1.161$ GeV data and 0.4 GeV for the $E_0 = 2.261$ GeV data. For the $E_0 = 4.461$ GeV data set, the relative change in the cross section was taken directly as an estimate of the momentum measurement uncertainty.

- Thanks to recent measurements of $R = \frac{\sigma_L}{\sigma_T}$ performed at Jefferson Lab [57], the precision of this quantity is greatly improved in our kinematic domain. Moreover, the structure function F_2 in the interesting kinematic range is not very sensitive to the value of R. In fact, even a 100% systematic uncertainty on R gives only a few

16

percent uncertainty on F_2.

$$\frac{\Delta F_2}{F_2}(x, Q^2) = \frac{1-\epsilon}{1+\epsilon R}\frac{\Delta R}{1+R} \approx R(1-\epsilon)\frac{\Delta R}{R} \quad . \tag{15}$$

Uncertainties of R given in Ref. [7] were propagated to F_2 and the corresponding systematic uncertainties were always lower than 5%.

All systematic uncertainties mentioned above and listed in Table 1 were combined in quadrature to give the total systematic uncertainty. When data sets from different beam energies overlapped, the systematic uncertainties were calculated as the central values using a weighted-average technique.

Table 1: Average systematic uncertainties for the three data sets for each of the different sources.

Source of uncertainty	Data set		
	$E_0 = 1.161$ GeV [%]	$E_0 = 2.261$ GeV [%]	$E_0 = 4.461$ GeV [%]
Normalization	3.2	1	1
Efficiency	3	3	3
Acceptance	6.6	4.7	7.7
e^+e^--pair production	0	0.001	0.05
e^- identification	0.04	0.4	0.2
Radiative correction	1.3	1.7	5
Momentum measurement	0.9	0.03	12
Uncertainty on $R = \frac{\sigma_L}{\sigma_T}$	2	1.2	0.5
Total	8.5	6.5	20

3.7. Moments of the Structure Function F_2

The non-zero mass of the target leads to an undesirable mixing between QCD operators of different spin in the OPE. To avoid this mixing in our analysis, we use Nachtmann [58] moments $M_n^{NM}(Q^2)$ instead of the usual (massless) Cornwall-Norton moments. The Nachtmann moments are defined as follows:

$$M_n^{NM}(Q^2) = \int_0^A dx \frac{\xi^{n+1}}{x^3} F_2(x, Q^2) \left[\frac{3 + 3(n+1)r + n(n+2)r^2}{(n+2)(n+3)}\right], \tag{16}$$

where $r = \sqrt{1 + 4M^2 x^2/Q^2}$, M is the nucleon mass and $\xi = 2x/(1+r)$. In the Bjorken limit $M^2/Q^2 \to 0$, the Nachtmann and Cornwall-Norton definitions coincide.

The carbon structure function moments were evaluated according to the method described in Refs. [6, 7]. The CLAS data were combined with the remaining world data on the structure function F_2, along with the inclusive cross section data from Refs. [10, 11, 12, 13, 14, 15, 16, 17, 18, 19, 20, 21, 22, 23, 24, 25, 26, 27, 28, 29, 30, 31, 32, 33, 34, 35] (see Fig. 1). The Q^2-range of the CLAS data, from 0.175 to 4.95 $(GeV/c)^2$, was divided into bins of width $\Delta Q^2 = 0.05$-0.1 $(GeV/c)^2$. Within each Q^2 bin, the world data were
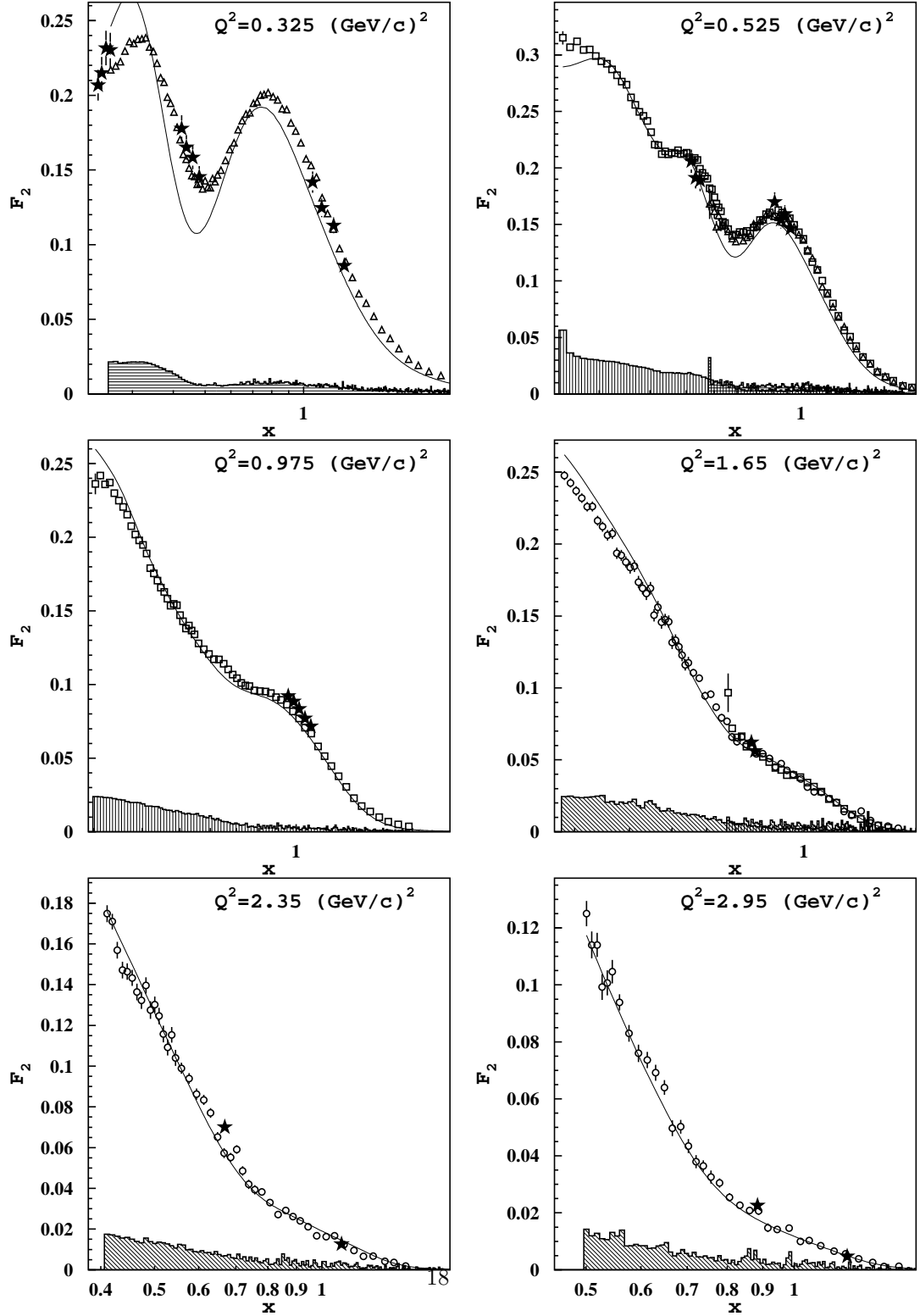
Figure 8: The carbon structure function $F_2(x, Q^2)$ per nucleon at six different Q^2 values. The open symbols represent experimental data obtained in the present analysis (triangles for $E_0 = 1.161$ GeV, squares for $E_0 = 2.261$ GeV and circles for $E_0 = 4.461$ GeV) with systematic uncertainties indicated by the hatched areas. The full stars show data from previous experiments [10, 11, 12, 13, 14, 15, 16, 17, 18, 19, 20, 21, 22]. The solid line represents the parametrization from Refs. [8, 48].
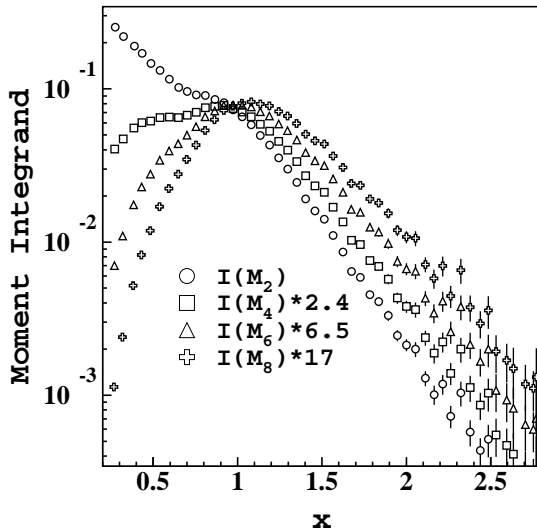
Figure 9: Integrands of the Nachtmann moments ($I(M_n)$) at $Q^2 = 0.825$ (GeV/c)^2: circles represent the integrand of M_2; squares show the integrand of M_4; triangles show the integrand of M_6; crosses show the integrand of M_8.

shifted to the central bin value Q_0^2, using the fit of $F_2(x, Q^2)$ from Refs. [8, 48]. The integrals of the data over x were performed numerically using the standard trapezoidal method TRAPER [59]. As an example, Fig. 9 shows the integrands of the first four moments as a function of x at fixed Q^2. The significance of the large x region for various moments can clearly be seen.

As in Refs. [6, 7], the world data at Q^2 above 5 (GeV/c)^2 were analyzed in the same way as described above, but with a different Q^2 bin size. The bin size was chosen to provide sufficient x-coverage for most of the Q^2 bins ($\Delta Q^2/Q^2 = 5$ %). The results, together with their statistical and systematic uncertainties, are shown in Fig. 10 and reported in Table 2. A comparison of Fig. 10 to the corresponding figures in Refs. [6, 7] shows the lack of the carbon data in the Q^2 interval from 5 to 40 (GeV/c)^2. This kinematic interval is very important because here moments reach the scaling regime.

The systematic uncertainty consists (see for example, Fig. 11) of experimental uncertainties in our data and the data given in Refs. [10, 11, 12, 13, 14, 15, 16, 17, 18, 19, 20, 21, 22, 23, 24, 25, 26, 27, 28, 29, 30, 31, 32, 33, 34, 35], and uncertainties in the evaluation procedure. The first type of uncertainties was accounted for in the moment evaluation point-by-point. To estimate them we had to account for the inclusion of many data sets measured in different laboratories with different detectors. In the present analysis, we assumed that the different experiments are independent and, therefore, only the systematic uncertainties within a given data set are correlated. The uncertainties in the evaluation procedure were obtained as described previously in Refs. [6, 7]. The lowest moment, $n = 2$, includes a systematic uncertainty due to the low-x extrapolation, which is negligible for larger n. To estimate this uncertainty we modified the parametrization from Refs. [8, 48], used for the low-x extrapolation. The modification, evaluated by a fit to the available carbon F_2 data in the low-x region, was given by the multiplicative

19
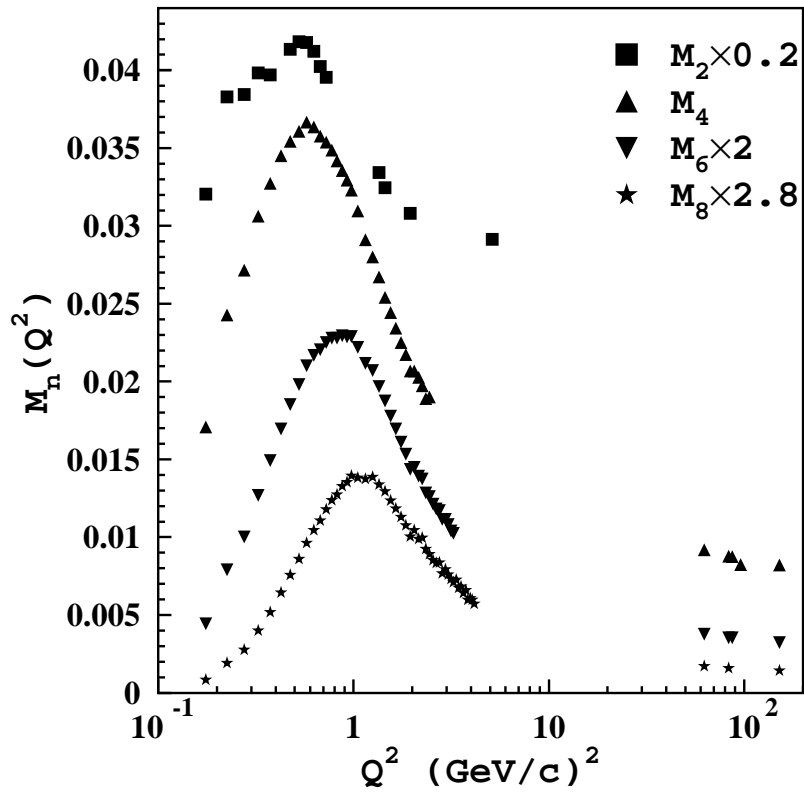
Figure 10: The Nachtmann moments extracted from the world data, including the new CLAS results. Uncertainties are statistical only and since their values do not exceed a few percent (see Table 2), they are smaller than the symbol size.
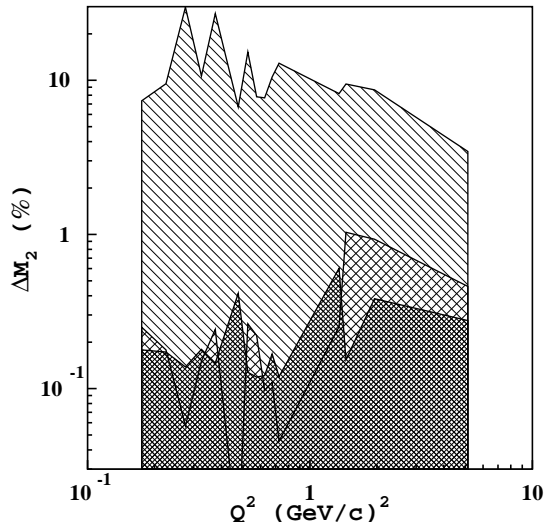
Figure 11: Uncertainties of the Nachtmann moment M_2 in percent. The lower cross-hatched area represents the statistical uncertainties. The left-hatched area represents the systematic uncertainties. The right-hatched area represents the low-x extrapolation uncertainty.

factor: $1 + (0.38 + 0.044/Q^2)x^{0.3}(1 - x)^{1.75}$. At $Q^2 = 1$ (GeV/c)^2 the relative change in the value of F_2 parametrization ranges from 2% at $x \sim 10^{-5}$ up to 18% at $x \sim 10^{-1}$. Then we compared the moments from the Table 2 with ones obtained by using the modified low-x extrapolation and we took the difference as the estimate of the systematic uncertainty. As one can see from Fig. 11, systematic uncertainties dominate at $n = 2$, while the statistical uncertainties become comparable at larger n.

4. Phenomenological Twists Expansion

The Q^2-distributions of the $n = 2, 4, 6$ and 8 moments were fit using the method developed in Refs. [6, 39, 60] with the following parametrization:

$$M_n(\alpha_S, Q^2) = \eta_n(\alpha_S) + HT_n(\alpha_S, Q^2) , \qquad (17)$$

where for $n \geq 4$ the leading-twist term contained only one unknown parameter due to the dominant non-singlet contribution, while for $n = 2$, both singlet and non-singlet terms were considered (for details see Refs. [6, 7]).

The higher-twist contribution is given by [61]:

$$HT_n(\alpha_S, Q^2) = \frac{\mu^2}{Q^2} \sum_{\tau=4}^{4+2N} A_{n\tau} \left\{ \frac{\alpha_s(Q^2)}{\alpha_s(\mu^2)} \right\}^{\gamma_{n\tau}} \left[\frac{\mu^2}{Q^2} \right]^{\frac{1}{2}(\tau-4)} , \qquad (18)$$

adding $2N$ free parameters $A_{n\tau}$ and $\gamma_{n\tau}$, with N being the number of higher-twist terms considered. Previous analyses [6, 7, 60] showed that it was necessary to take $N \geq 2$ when $n \geq 4$, while for $n = 2$ it was sufficient to have $N \geq 1$. In principle, the number

21

Table 2: The Nachtmann moments for $n = 2, 4, 6$ and 8 evaluated in the interval $0.15 \leq Q^2 \leq 150$ (GeV/c)^2. The moments are labeled with an asterisk when the contribution to the integral by the experimental data is between 50% and 70%. All the others were evaluated with more than 70% data coverage. The data are reported together with the statistical and systematic uncertainties, the third uncertainty for $n = 2$ is due to the low-x extrapolation.

Q^2 [(GeV/c)^2]	$M_2(Q^2)$x10^{-1}	$M_4(Q^2)$x10^{-2}	$M_6(Q^2)$x10^{-2}	$M_8(Q^2)$x10^{-3}
0.175	$1.602 \pm 0.003 \pm 0.126 \pm 0.004$	$1.707 \pm 0.004 \pm 0.133$	$0.222 \pm 0.001 \pm 0.018$	$0.302 \pm 0.001 \pm 0.027$
0.225	$1.915 \pm 0.003 \pm 0.223 \pm 0.003$	$2.428 \pm 0.007 \pm 0.179$	$0.395 \pm 0.002 \pm 0.029$	$0.687 \pm 0.003 \pm 0.051$
0.275	$1.923 \pm 0.003 \pm 0.645 \pm 0.001$	$2.715 \pm 0.005 \pm 0.303$	$0.500 \pm 0.001 \pm 0.045$	$0.990 \pm 0.002 \pm 0.092$
0.325	$1.991 \pm 0.004 \pm 0.256 \pm 0.003$	$3.063 \pm 0.006 \pm 0.198$	$0.635 \pm 0.001 \pm 0.040$	$1.424 \pm 0.004 \pm 0.100$
0.375	$1.985 \pm 0.003 \pm 0.592 \pm 0.005$	$3.273 \pm 0.007 \pm 0.271$	$0.746 \pm 0.002 \pm 0.044$	$1.854 \pm 0.006 \pm 0.111$
0.425		$3.452 \pm 0.008 \pm 0.215$	$0.847 \pm 0.002 \pm 0.057$	$2.298 \pm 0.008 \pm 0.180$
0.475	$2.067 \pm 0.009 \pm 0.145 \pm 0.000$	$3.544 \pm 0.009 \pm 0.219$	$0.926 \pm 0.003 \pm 0.059$	$2.707 \pm 0.011 \pm 0.188$
0.525	$2.091 \pm 0.003 \pm 0.391 \pm 0.005$	$3.608 \pm 0.008 \pm 0.231$	$0.990 \pm 0.003 \pm 0.062$	$3.073 \pm 0.011 \pm 0.222$
0.575	$2.090 \pm 0.002 \pm 0.176 \pm 0.005$	$3.667 \pm 0.008 \pm 0.194$	$1.051 \pm 0.003 \pm 0.057$	$3.435 \pm 0.013 \pm 0.216$
0.625	$2.061 \pm 0.002 \pm 0.150 \pm 0.002$	$3.636 \pm 0.009 \pm 0.209$	$1.085 \pm 0.004 \pm 0.065$	$3.730 \pm 0.017 \pm 0.260$
0.675	$2.011 \pm 0.003 \pm 0.254 \pm 0.002$	$3.577 \pm 0.010 \pm 0.225$	$1.102 \pm 0.005 \pm 0.067$	$3.949 \pm 0.024 \pm 0.276$
0.725	$1.977 \pm 0.002 \pm 0.326 \pm 0.001$	$3.537 \pm 0.010 \pm 0.242$	$1.125 \pm 0.005 \pm 0.072$	$4.208 \pm 0.028 \pm 0.313$
0.775		$3.488 \pm 0.011 \pm 0.213$	$1.139 \pm 0.006 \pm 0.069$	$4.417 \pm 0.034 \pm 0.324$
0.825		$3.418 \pm 0.009 \pm 0.205$	$1.139 \pm 0.004 \pm 0.072$	$4.545 \pm 0.024 \pm 0.332$
0.875		$3.357 \pm 0.008 \pm 0.201$	$1.148 \pm 0.005 \pm 0.074$	$4.741 \pm 0.027 \pm 0.369$
0.925		$3.295 \pm 0.008 \pm 0.327$	$1.143 \pm 0.005 \pm 0.082$	$4.835 \pm 0.027 \pm 0.405$
0.975		$3.230 \pm 0.009 \pm 0.229$	$1.144 \pm 0.005 \pm 0.066$	$4.976 \pm 0.030 \pm 0.289$

Q^2 [(GeV/c)^2]	$M_2(Q^2)$x10^{-1}	$M_4(Q^2)$x10^{-2}	$M_6(Q^2)$x10^{-2}	$M_8(Q^2)$x10^{-3}
1.050		3.097 ± 0.006 ± 0.205	1.109 ± 0.004 ± 0.065	4.936 ± 0.023 ± 0.277
1.150		2.911 ± 0.007 ± 0.234	1.058 ± 0.004 ± 0.077	4.911 ± 0.029 ± 0.402
1.250		2.799 ± 0.007 ± 0.259	1.035 ± 0.005 ± 0.081	4.957 ± 0.035 ± 0.429
1.350	1.672 ± 0.010 ± 0.130 ± 0.004	2.673 ± 0.007 ± 0.221	0.984 ± 0.004 ± 0.080	4.778 ± 0.034 ± 0.421
1.450	*1.622 ± 0.002 ± 0.141 ± 0.017	2.541 ± 0.008 ± 0.215	0.938 ± 0.005 ± 0.076	4.627 ± 0.034 ± 0.385
1.550		2.443 ± 0.008 ± 0.254	0.889 ± 0.005 ± 0.081	4.408 ± 0.039 ± 0.416
1.650		2.343 ± 0.008 ± 0.267	0.847 ± 0.005 ± 0.083	4.232 ± 0.036 ± 0.437
1.750		2.250 ± 0.009 ± 0.238	0.805 ± 0.005 ± 0.089	4.033 ± 0.038 ± 0.489
1.850		2.174 ± 0.010 ± 0.244	0.766 ± 0.005 ± 0.096	3.844 ± 0.040 ± 0.575
1.950	*1.540 ± 0.006 ± 0.114 ± 0.014	2.067 ± 0.010 ± 0.221	0.718 ± 0.005 ± 0.085	3.582 ± 0.036 ± 0.473
2.050		2.068 ± 0.012 ± 0.235	0.725 ± 0.007 ± 0.096	3.731 ± 0.047 ± 0.570
2.150		2.027 ± 0.012 ± 0.257	0.696 ± 0.007 ± 0.098	3.533 ± 0.050 ± 0.586
2.250		1.974 ± 0.013 ± 0.228	0.687 ± 0.008 ± 0.105	3.560 ± 0.066 ± 0.663
2.350		1.891 ± 0.013 ± 0.225	0.642 ± 0.009 ± 0.113	3.300 ± 0.080 ± 0.791
2.450		1.901 ± 0.013 ± 0.424	0.630 ± 0.009 ± 0.130	3.180 ± 0.087 ± 0.814
2.550			0.605 ± 0.008 ± 0.096	3.042 ± 0.065 ± 0.614
2.650			0.590 ± 0.009 ± 0.104	2.983 ± 0.082 ± 0.721
2.750			0.585 ± 0.009 ± 0.092	2.986 ± 0.075 ± 0.615
2.850			0.557 ± 0.008 ± 0.104	2.741 ± 0.069 ± 0.643
2.950			0.557 ± 0.009 ± 0.094	2.831 ± 0.082 ± 0.603

Q^2 [(GeV/c)^2]	$M_2(Q^2)$x10^{-1}	$M_4(Q^2)$x10^{-2}	$M_6(Q^2)$x10^{-2}	$M_8(Q^2)$x10^{-3}
3.050			$0.540 \pm 0.009 \pm 0.095$	$2.717 \pm 0.075 \pm 0.611$
3.150			$0.520 \pm 0.008 \pm 0.092$	$2.616 \pm 0.075 \pm 0.601$
3.250			$0.513 \pm 0.008 \pm 0.103$	$2.536 \pm 0.070 \pm 0.642$
3.350				$2.597 \pm 0.068 \pm 0.655$
3.450				$2.409 \pm 0.069 \pm 0.579$
3.550				$2.437 \pm 0.056 \pm 0.747$
3.650				$2.295 \pm 0.078 \pm 0.765$
3.750				$2.354 \pm 0.072 \pm 0.613$
3.850				$2.137 \pm 0.063 \pm 0.589$
3.950				$2.170 \pm 0.064 \pm 0.599$
4.050				$2.132 \pm 0.072 \pm 0.557$
4.150				$2.038 \pm 0.071 \pm 0.692$
5.125	*$1.457 \pm 0.004 \pm 0.047 \pm 0.007$			
62.500		$0.920 \pm 0.007 \pm 0.023$	$0.189 \pm 0.002 \pm 0.002$	$0.608 \pm 0.009 \pm 0.009$
83.250		$0.877 \pm 0.009 \pm 0.016$	$0.177 \pm 0.003 \pm 0.001$	$0.561 \pm 0.010 \pm 0.007$
87.000		*$0.874 \pm 0.007 \pm 0.026$	$0.176 \pm 0.002 \pm 0.007$	
96.000		*$0.824 \pm 0.011 \pm 0.030$		
151.500		*$0.821 \pm 0.015 \pm 0.018$	$0.162 \pm 0.005 \pm 0.001$	$0.512 \pm 0.020 \pm 0.003$

Table 3: Extracted parameters of the twist expansion at the reference scale $\mu^2 = 10$ (GeV/c)^2. The first uncertainty has a statistical origin and is obtained from a MINOS [59] minimization procedure, while the second uncertainty is the systematic one described in text. The contribution of twist-6 to M_2 was too small to be extracted by the present procedure.

n	2	4	6	8
$\eta_n(\mu^2)$	$0.1411\pm0.0005\pm0.0050$	$(1.206\pm0.008\pm0.051)\times10^{-2}$	$(2.79\pm0.05\pm0.07)\times10^{-3}$	$(9.7\pm0.5\pm0.3)\times10^{-4}$
A_{n4}	$(0.6\pm1.8\pm1.1)\times10^{-6}$	$(2.14\pm0.02\pm2.68)\times10^{-4}$	$(2.22\pm0.03\pm3.25)\times10^{-4}$	$(2.9\pm0.1\pm2.7)\times10^{-4}$
γ_{n4}	$8\pm3\pm10$	$4.95\pm0.01\pm1.65$	$5.21\pm0.02\pm4.75$	$3.7\pm0.1\pm2.1$
A_{n6}	-	$(-4.65\pm0.04\pm5.07)\times10^{-5}$	$(-6.2\pm0.1\pm5.5)\times10^{-5}$	$(-7.5\pm0.4\pm4.1)\times10^{-5}$
γ_{n6}	-	$3.83\pm0.01\pm1.58$	$3.84\pm0.02\pm2.21$	$2.5\pm0.1\pm1.9$

of higher-twist terms N should be infinite, but as was shown in Ref. [62], already the minimum number of terms (i.e. $N = 1$ for $n = 2$ and $N = 2$ when $n \geq 4$) completely described the total higher-twist contribution. Adding further terms does not change the obtained separation between leading and higher twists. Hence, in the present analysis we used $N = 1$ for $n = 2$ and $N = 2$ when $n \geq 4$.

The higher-twist parameters $\gamma_{n\tau}$ are effectively the LO anomalous dimensions of the perturbative Wilson coefficients $E_{n\tau}(\mu_r, \mu_f, \alpha_S)$ in Eq. 2, while the parameters $A_{n\tau}$ are proportional to the matrix elements of QCD operators $O_{n\tau}(\mu)$. Higher-twist operators get mixed and only leading-twist parameters A_{n2} can be directly related to the operators $O_{n2}(\mu)$ for $\tau > 2$ since pQCD calculations of $\gamma_{n\tau}$ are at present unavailable.

Based on the above, the n-th moment (see Eq. 18) for $n \geq 4$ has five unknown parameters: the leading-twist parameter A_{n2} and the higher-twist parameters A_{n4}, γ_{n4}, A_{n6} and γ_{n6}. These parameters were simultaneously determined from a χ^2-minimization procedure (MINUIT [63]) over the allowed Q^2 range. The statistical uncertainties of the experimental moments were used by MINOS [63] to obtain statistical uncertainties on the extracted parameters. Their systematic uncertainties were obtained by adding/subtracting the systematic uncertainties to the experimental moments and by repeating the twist extraction procedure.

In the case of $n = 2$, the sum of the non-singlet and singlet terms at the leading twist was considered, therefore adding the leading-twist parameter due to the gluon moment at the reference scale. Moreover, due to the vanishing contribution of the higher twists in M_2 (see Fig. 12), we considered the twist-4 term only.

The fit results are shown in Fig. 12, while in Table 3, we report the parameter values obtained at the reference scale $\mu^2 = 10$ (GeV/c)^2. In addition, the extracted leading-twist contribution is reported in Table 4.

5. Comparison to Deuteron

Once the separation between the leading and higher-twist terms is obtained, we can compare them to the corresponding terms in the deuteron. The deuteron, being a loosely bound system, is considered here as representing structure function moments of an almost free proton and neutron.

In Fig. 13 the ratio of the leading-twist moments of carbon-to-deuteron is shown with its statistical and systematic uncertainties. It is compared to the ratio of the
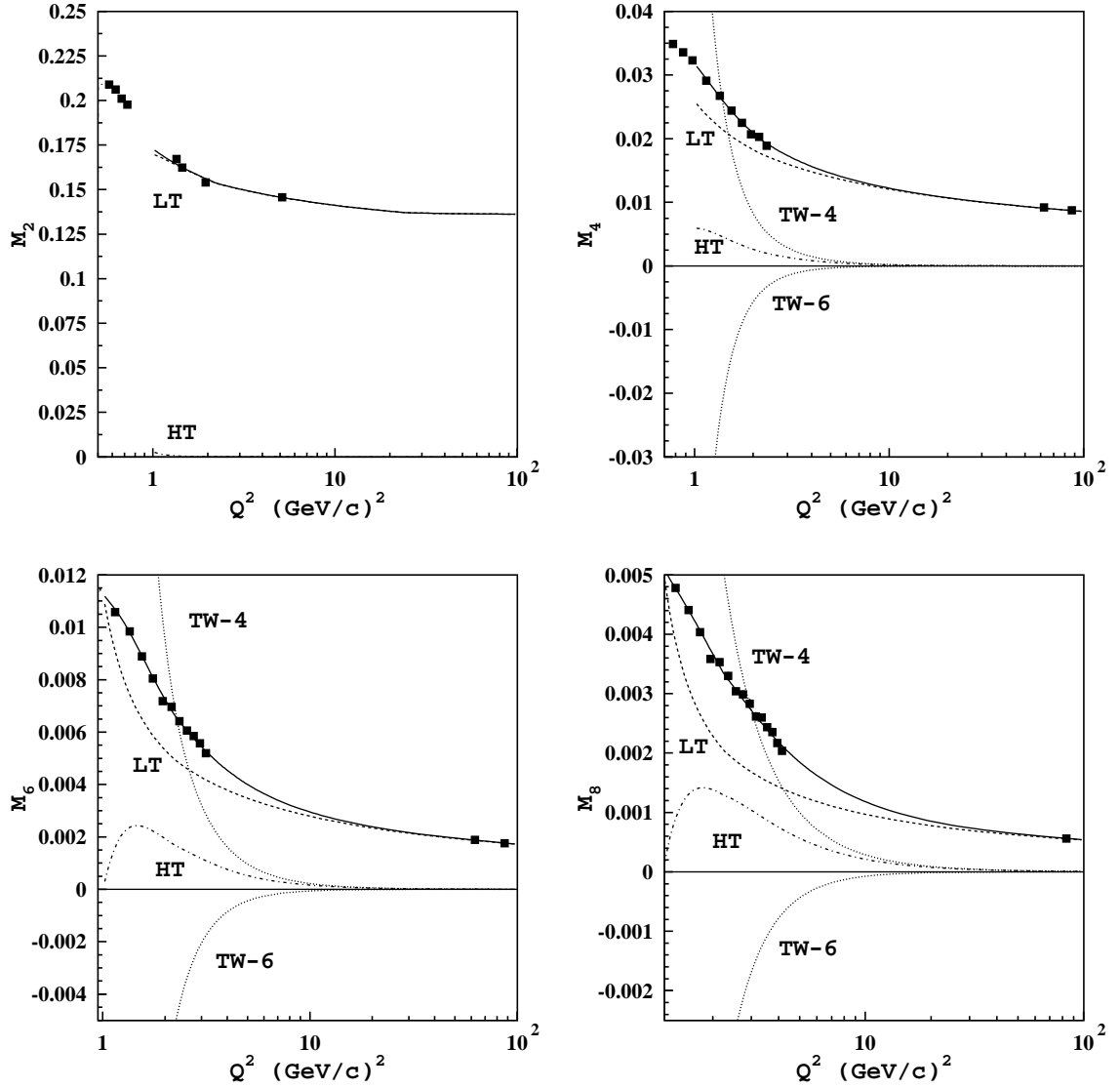
Figure 12: Results of the twist analysis. The squares represent the Nachtmann moments obtained in this analysis. The solid line is the fit to the moments using Eq. 17 with the parameters listed in Table 3. The leading-twist (LT), twist-4 (TW-4), twist-6 (TW-6) and the total higher twist (HT) contributions to the fit are indicated.

26

Table 4: The extracted leading-twist contribution $\eta_n(Q^2)$ shown in Fig. 12, reported with systematic uncertainties.

Q^2 [(GeV/c)^2]	$\eta_2(Q^2)$x10^{-1}	$\eta_4(Q^2)$x10^{-2}	$\eta_6(Q^2)$x10^{-3}	$\eta_8(Q^2)$x10^{-3}
1.025	1.694 ± 0.004	2.54 ± 0.02	10.88 ± 0.20	7.97 ± 0.39
1.075	1.685 ± 0.004	2.47 ± 0.02	10.03 ± 0.18	6.72 ± 0.33
1.125	1.675 ± 0.003	2.40 ± 0.02	9.35 ± 0.17	5.85 ± 0.28
1.175	1.666 ± 0.003	2.34 ± 0.02	8.80 ± 0.16	5.21 ± 0.25
1.225	1.657 ± 0.003	2.29 ± 0.02	8.33 ± 0.15	4.71 ± 0.23
1.275	1.648 ± 0.003	2.24 ± 0.02	7.93 ± 0.14	4.32 ± 0.21
1.325	1.640 ± 0.003	2.19 ± 0.02	7.59 ± 0.14	4.00 ± 0.19
1.375	1.632 ± 0.003	2.15 ± 0.01	7.29 ± 0.13	3.74 ± 0.18
1.425	1.624 ± 0.002	2.11 ± 0.01	7.03 ± 0.13	3.52 ± 0.17
1.475	1.616 ± 0.002	2.08 ± 0.01	6.80 ± 0.12	3.33 ± 0.16
1.525	1.609 ± 0.002	2.05 ± 0.01	6.59 ± 0.12	3.17 ± 0.15
1.575	1.602 ± 0.002	2.02 ± 0.01	6.40 ± 0.11	3.02 ± 0.14
1.625	1.596 ± 0.002	1.99 ± 0.01	6.23 ± 0.11	2.90 ± 0.14
1.675	1.590 ± 0.002	1.96 ± 0.01	6.07 ± 0.11	2.79 ± 0.13
1.725	1.584 ± 0.002	1.94 ± 0.01	5.93 ± 0.11	2.69 ± 0.13
1.775	1.578 ± 0.002	1.91 ± 0.01	5.80 ± 0.10	2.60 ± 0.12
1.825	1.572 ± 0.002	1.89 ± 0.01	5.68 ± 0.10	2.51 ± 0.12
1.875	1.567 ± 0.002	1.87 ± 0.01	5.56 ± 0.10	2.44 ± 0.12
1.925	1.562 ± 0.002	1.85 ± 0.01	5.46 ± 0.10	2.37 ± 0.11
1.975	1.557 ± 0.002	1.83 ± 0.01	5.36 ± 0.09	2.31 ± 0.11
2.025	1.552 ± 0.002	1.81 ± 0.01	5.27 ± 0.09	2.25 ± 0.11
2.075	1.548 ± 0.002	1.80 ± 0.01	5.18 ± 0.09	2.20 ± 0.10
2.125	1.543 ± 0.002	1.78 ± 0.01	5.10 ± 0.09	2.15 ± 0.10
2.175	1.539 ± 0.002	1.76 ± 0.01	5.02 ± 0.09	2.10 ± 0.10
2.225	1.535 ± 0.002	1.75 ± 0.01	4.95 ± 0.09	2.06 ± 0.10
2.275	1.532 ± 0.002	1.74 ± 0.01	4.89 ± 0.09	2.02 ± 0.10
2.325	1.529 ± 0.002	1.72 ± 0.01	4.83 ± 0.08	1.99 ± 0.09
2.375	1.527 ± 0.002	1.71 ± 0.01	4.78 ± 0.08	1.96 ± 0.09

Q^2 [(GeV/c)^2]	$\eta_2(Q^2)$x10^{-1}	$\eta_4(Q^2)$x10^{-2}	$\eta_6(Q^2)$x10^{-3}	$\eta_8(Q^2)$x10^{-3}
2.425	1.524 ± 0.002	1.70 ± 0.01	4.73 ± 0.08	1.93 ± 0.09
2.475	1.522 ± 0.002	1.69 ± 0.01	4.68 ± 0.08	1.90 ± 0.09
2.525	1.520 ± 0.002	1.68 ± 0.01	4.63 ± 0.08	1.88 ± 0.09
2.575	1.518 ± 0.002	1.67 ± 0.01	4.59 ± 0.08	1.85 ± 0.09
2.625	1.516 ± 0.002	1.66 ± 0.01	4.54 ± 0.08	1.83 ± 0.09
2.675	1.514 ± 0.002	1.65 ± 0.01	4.50 ± 0.08	1.80 ± 0.08
2.725	1.512 ± 0.002	1.64 ± 0.01	4.46 ± 0.08	1.78 ± 0.08
2.775	1.510 ± 0.002	1.63 ± 0.01	4.42 ± 0.08	1.76 ± 0.08
2.825	1.508 ± 0.002	1.62 ± 0.01	4.39 ± 0.08	1.74 ± 0.08
2.875	1.506 ± 0.002	1.61 ± 0.01	4.35 ± 0.08	1.72 ± 0.08
2.925	1.504 ± 0.003	1.61 ± 0.01	4.32 ± 0.08	1.70 ± 0.08
2.975	1.503 ± 0.003	1.60 ± 0.01	4.28 ± 0.07	1.69 ± 0.08
3.025	1.501 ± 0.003	1.59 ± 0.01	4.25 ± 0.07	1.67 ± 0.08
3.075	1.499 ± 0.003	1.58 ± 0.01	4.22 ± 0.07	1.65 ± 0.08
3.125	1.498 ± 0.003	1.58 ± 0.01	4.19 ± 0.07	1.64 ± 0.08
3.175	1.496 ± 0.003	1.57 ± 0.01	4.16 ± 0.07	1.62 ± 0.08
3.225	1.495 ± 0.003	1.56 ± 0.01	4.13 ± 0.07	1.61 ± 0.07
3.275	1.493 ± 0.003	1.56 ± 0.01	4.10 ± 0.07	1.59 ± 0.07
3.325	1.492 ± 0.003	1.55 ± 0.01	4.08 ± 0.07	1.58 ± 0.07
3.375	1.490 ± 0.003	1.54 ± 0.01	4.05 ± 0.07	1.56 ± 0.07
3.425	1.489 ± 0.003	1.54 ± 0.01	4.02 ± 0.07	1.55 ± 0.07
3.475	1.488 ± 0.003	1.53 ± 0.01	4.00 ± 0.07	1.54 ± 0.07
3.525	1.486 ± 0.003	1.52 ± 0.01	3.98 ± 0.07	1.53 ± 0.07
3.575	1.485 ± 0.003	1.52 ± 0.01	3.95 ± 0.07	1.51 ± 0.07
3.625	1.484 ± 0.003	1.51 ± 0.01	3.93 ± 0.07	1.50 ± 0.07
3.675	1.482 ± 0.003	1.51 ± 0.01	3.91 ± 0.07	1.49 ± 0.07
3.725	1.481 ± 0.003	1.50 ± 0.01	3.89 ± 0.07	1.48 ± 0.07
3.775	1.480 ± 0.003	1.50 ± 0.01	3.87 ± 0.07	1.47 ± 0.07
3.825	1.479 ± 0.003	1.49 ± 0.01	3.84 ± 0.07	1.46 ± 0.07
3.875	1.478 ± 0.003	1.49 ± 0.01	3.82 ± 0.07	1.45 ± 0.07

Q^2 [(GeV/c)^2]	$\eta_2(Q^2)$x10^{-1}	$\eta_4(Q^2)$x10^{-2}	$\eta_6(Q^2)$x10^{-3}	$\eta_8(Q^2)$x10^{-3}
3.925	1.477 ± 0.003	1.48 ± 0.01	3.81 ± 0.07	1.44 ± 0.07
3.975	1.476 ± 0.003	1.48 ± 0.01	3.79 ± 0.07	1.43 ± 0.07
4.025	1.474 ± 0.003	1.47 ± 0.01	3.77 ± 0.07	1.42 ± 0.07
4.075	1.473 ± 0.003	1.47 ± 0.01	3.75 ± 0.06	1.41 ± 0.07
4.125	1.472 ± 0.003	1.46 ± 0.01	3.73 ± 0.06	1.40 ± 0.06
4.175	1.471 ± 0.003	1.46 ± 0.01	3.71 ± 0.06	1.40 ± 0.06
4.225	1.470 ± 0.003	1.45 ± 0.01	3.70 ± 0.06	1.39 ± 0.06
4.275	1.469 ± 0.004	1.45 ± 0.01	3.68 ± 0.06	1.38 ± 0.06
4.325	1.468 ± 0.004	1.45 ± 0.01	3.66 ± 0.06	1.37 ± 0.06
4.375	1.467 ± 0.004	1.44 ± 0.01	3.65 ± 0.06	1.36 ± 0.06
4.425	1.467 ± 0.004	1.44 ± 0.01	3.63 ± 0.06	1.35 ± 0.06
4.475	1.466 ± 0.004	1.43 ± 0.01	3.62 ± 0.06	1.35 ± 0.06
4.525	1.465 ± 0.004	1.43 ± 0.01	3.60 ± 0.06	1.34 ± 0.06
4.575	1.464 ± 0.004	1.43 ± 0.01	3.59 ± 0.06	1.33 ± 0.06
4.625	1.463 ± 0.004	1.42 ± 0.01	3.57 ± 0.06	1.33 ± 0.06
4.675	1.462 ± 0.004	1.42 ± 0.01	3.56 ± 0.06	1.32 ± 0.06
4.725	1.461 ± 0.004	1.41 ± 0.01	3.54 ± 0.06	1.31 ± 0.06
4.775	1.460 ± 0.004	1.41 ± 0.01	3.53 ± 0.06	1.31 ± 0.06
4.825	1.460 ± 0.004	1.41 ± 0.01	3.52 ± 0.06	1.30 ± 0.06
4.875	1.459 ± 0.004	1.40 ± 0.01	3.50 ± 0.06	1.29 ± 0.06
4.925	1.458 ± 0.004	1.40 ± 0.01	3.49 ± 0.06	1.29 ± 0.06
4.975	1.457 ± 0.004	1.40 ± 0.01	3.48 ± 0.06	1.28 ± 0.06
5.025	1.456 ± 0.004	1.39 ± 0.01	3.47 ± 0.06	1.27 ± 0.06
5.075	1.456 ± 0.004	1.39 ± 0.01	3.45 ± 0.06	1.27 ± 0.06
5.125	1.455 ± 0.004	1.39 ± 0.01	3.44 ± 0.06	1.26 ± 0.06
5.275	1.453 ± 0.004	1.38 ± 0.01	3.41 ± 0.06	1.25 ± 0.06
5.325	1.452 ± 0.004	1.37 ± 0.01	3.40 ± 0.06	1.24 ± 0.06
5.375	1.451 ± 0.004	1.37 ± 0.01	3.38 ± 0.06	1.24 ± 0.06
5.475	1.450 ± 0.004	1.37 ± 0.01	3.36 ± 0.06	1.23 ± 0.06
5.525	1.449 ± 0.004	1.36 ± 0.01	3.35 ± 0.06	1.22 ± 0.06

Q^2 $[(\text{GeV/c})^2]$	$\eta_2(Q^2)\text{x}10^{-1}$	$\eta_4(Q^2)\text{x}10^{-2}$	$\eta_6(Q^2)\text{x}10^{-3}$	$\eta_8(Q^2)\text{x}10^{-3}$
5.625	1.448 ± 0.004	1.36 ± 0.009	3.33 ± 0.06	1.21 ± 0.06
5.675	1.447 ± 0.004	1.35 ± 0.009	3.32 ± 0.06	1.21 ± 0.05
5.725	1.447 ± 0.004	1.35 ± 0.009	3.31 ± 0.06	1.20 ± 0.05
5.955	1.444 ± 0.004	1.34 ± 0.009	3.27 ± 0.06	1.18 ± 0.05
6.915	1.434 ± 0.005	1.30 ± 0.009	3.11 ± 0.05	1.11 ± 0.05
7.267	1.431 ± 0.005	1.28 ± 0.008	3.06 ± 0.05	1.09 ± 0.05
7.630	1.427 ± 0.005	1.27 ± 0.008	3.02 ± 0.05	1.07 ± 0.05
8.021	1.424 ± 0.005	1.26 ± 0.008	2.97 ± 0.05	1.05 ± 0.05
8.847	1.418 ± 0.005	1.23 ± 0.008	2.89 ± 0.05	1.01 ± 0.05
9.775	1.413 ± 0.005	1.21 ± 0.008	2.80 ± 0.05	0.97 ± 0.04
10.267	1.410 ± 0.005	1.20 ± 0.008	2.77 ± 0.05	0.95 ± 0.04
10.762	1.407 ± 0.005	1.18 ± 0.008	2.73 ± 0.05	0.94 ± 0.04
11.344	1.405 ± 0.005	1.17 ± 0.008	2.69 ± 0.05	0.92 ± 0.04
12.580	1.399 ± 0.006	1.15 ± 0.008	2.62 ± 0.04	0.89 ± 0.04
13.238	1.397 ± 0.006	1.14 ± 0.007	2.58 ± 0.04	0.88 ± 0.04
14.689	1.392 ± 0.006	1.12 ± 0.007	2.52 ± 0.04	0.85 ± 0.04
17.108	1.385 ± 0.006	1.09 ± 0.007	2.42 ± 0.04	0.81 ± 0.04
19.072	1.380 ± 0.006	1.07 ± 0.007	2.36 ± 0.04	0.78 ± 0.03
20.108	1.378 ± 0.006	1.06 ± 0.007	2.33 ± 0.04	0.77 ± 0.03
21.097	1.376 ± 0.006	1.05 ± 0.007	2.31 ± 0.04	0.76 ± 0.03
24.259	1.370 ± 0.006	1.03 ± 0.007	2.23 ± 0.04	0.73 ± 0.03
26.680	1.369 ± 0.007	1.01 ± 0.007	2.19 ± 0.04	0.71 ± 0.03
32.500	1.367 ± 0.007	0.99 ± 0.006	2.10 ± 0.03	0.68 ± 0.03
34.932	1.367 ± 0.007	0.98 ± 0.006	2.07 ± 0.03	0.67 ± 0.03
36.750	1.366 ± 0.007	0.97 ± 0.006	2.05 ± 0.03	0.66 ± 0.03
43.970	1.365 ± 0.007	0.94 ± 0.006	1.99 ± 0.03	0.63 ± 0.03
47.440	1.365 ± 0.007	0.93 ± 0.006	1.96 ± 0.03	0.62 ± 0.03
64.270	1.363 ± 0.007	0.90 ± 0.006	1.85 ± 0.03	0.58 ± 0.02
75.000	1.363 ± 0.007	0.88 ± 0.006	1.80 ± 0.03	0.56 ± 0.02
86.000	1.362 ± 0.007	0.87 ± 0.006	1.76 ± 0.03	0.55 ± 0.02
97.690	1.362 ± 0.007	0.85 ± 0.005	1.72 ± 0.03	0.53 ± 0.02

corresponding structure functions obtained in Ref. [35] and satisfied the cut $Q^2 > 25$ $(\text{GeV/c})^2$, ensuring leading-twist dominance.

Considering Fermi motion effects only, and applying the Impulse Approximation (IA) [64, 65]:

$$F_2^A(x, Q^2) = \int_x^{M_A/M} dz\, f^A(z)\, F_2^N\left(\frac{x}{z}, Q^2\right) \quad , \tag{19}$$

where $f^A(z)$ is the non-relativistic nucleon (light-cone) momentum distribution in the nucleus and the superscripts A and N are introduced to distinguish the nuclear (A) and nucleon (N) distributions. Then, if we define the n-th moment of the distribution $f^A(z)$ by:

$$\mathcal{F}_n^A = \int_0^{M_A/M} dz\, z^{n-1} f^A(z) \, , \tag{20}$$

in the moment space, the convolution becomes the product of the moments [66]:

$$M_n^A(Q^2) = \mathcal{F}_n^A M_n^N(Q^2) \, . \tag{21}$$

This leads to a simple relation between the carbon and deuteron moments in the IA:

$$\frac{M_n^C(Q^2)}{M_n^D(Q^2)} = \frac{\mathcal{F}_n^C}{\mathcal{F}_n^D} \, , \tag{22}$$

where the nucleon structure function moments are canceled. Therefore, in the IA the ratio of nuclear structure function moments is reduced to the ratio of the nucleon momentum distribution moments. This ratio, obtained with nuclear wave functions from Refs. [48, 67], is shown in Fig. 13 by the solid line. The deviation of the data points from the curve at large n is the consequence of the EMC effect. Indeed, the ratio of the moments is in good agreement with the ratio of the structure functions taken at x values corresponding to the average $<x>_n$ for a given n defined as in Ref. [68]. Hence, in the moment space, we confirm the EMC effect discovered previously in x-space.

A similar ratio of the carbon to deuteron moments, but for the total higher-twist contribution taken at $Q^2 = 2$ $(\text{GeV/c})^2$, is shown in Fig. 14. The curve representing the Fermi motion expectation is the same as for the leading-twist case. The higher-twist ratio is very different from the ratio of leading twists. Surprisingly, for small $n < 8$, the total higher-twist contribution in complex nuclei is smaller than in the deuteron. Despite the large systematic uncertainties, the ratio rises with n almost linearly, surpassing unity at $n \approx 7$. This behavior is clearly not related to the Fermi motion of nucleons in the nucleus. Naively one may expect an overall larger total higher-twist contribution in complex nuclei because of additional processes, e.g. nuclear FSI and SRC [52, 53, 69], which are less important in the deuteron. A hint of this suppression of the higher twists in nuclei was already observed in Ref. [8], where the authors tried to connect it to the suppression of the nucleon excited state form-factors in nuclei [70, 2]. Indeed, looking at the resonance peaks in the free proton, deuteron and carbon, shown in Fig. 15, one may conclude that they disappear in nuclei. However, the suppression factors extracted in Ref. [2] would lead to a much larger difference between the carbon and deuteron moments. This is because the total resonance contribution to the structure function moments in the few $(\text{GeV/c})^2$ domain is very important [4]. Thus, if resonance form-factors are really
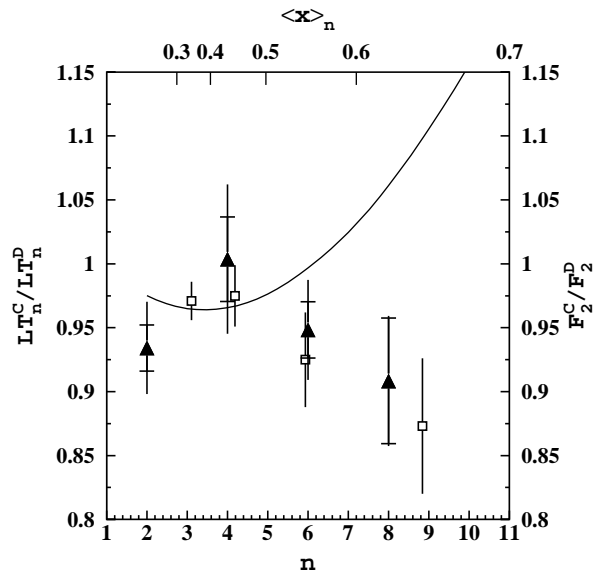
Figure 13: The carbon-to-deuteron ratio of the leading-twist moments (full triangles) compared with the ratio of corresponding structure functions obtained in Ref. [35] (open squares) taken at average $<x>_n$ values (the cut $Q^2 > 25$ $(GeV/c)^2$ is applied to avoid higher-twist contamination in the structure function ratio). The curve shows the theoretical expectation due to Fermi motion effects. Internal error bars are statistical only and the total error bars are the statistical and systematic uncertainties summed in quadrature.

suppressed in nuclei, this has to be compensated by an almost equivalent increase of the non-resonant contribution to the first four moments.

One explanation of the EMC effect as due to partial quark deconfinement for a nucleon embedded in nuclear matter was suggested within the rescaling model proposed in Ref. [71]. In Ref. [8] it was also connected to the higher-twist suppression in nuclei. In fact, if one considers the normal QCD potential, partons inside the nucleon will interact more strongly when approaching the nucleon radius, while partons deep inside the nucleon will behave as free particles. This intuitive picture is the basis for the MIT Bag model [72]. The discussion below is a simple-minded speculation suggested by this picture.

The interaction of the struck parton with the rest of the nucleon will result in the appearance of higher twists, but as long as the parton is located in the central region of the nucleon, it will propagate as a free particle, resulting in the leading-twist dominance. Therefore, for a given x (or alternatively n in the moment space), the Q^2 value at which the higher-twist contribution becomes significant Q^2_{HT} can be considered as the inverse of the mean free path of the struck parton:

$$\lambda_q \sim r_N \sqrt{\frac{M^2}{Q^2_{HT}}},$$

(23)

where the nucleon charge radius r_N and nucleon mass M define the characteristic scale. An increase of the nucleon radius as in the model of Ref. [71] would lead to a shift of the higher-twist contribution to lower Q^2 for all n. Both observed ratios of the leading and higher twists are compatible with such a naive picture. One can combine these observations together to visualize the spatial distribution of the free partons inside the nucleon as shown in Fig. 16. Here we defined Q^2_{HT} used in Eq. 23 as the Q^2 value at which the total higher-twist contribution in the given nth moment reaches 5% of the leading twist. As one can see in the nucleon bound inside the carbon nucleus, partons have a larger free propagation range, but the amount of highly energetic free partons is decreased, keeping the integrated strength almost constant.

6. Conclusions

A measurement of inclusive electron scattering by a carbon nucleus was performed in a wide two-dimensional range of x and Q^2. This measurement improves the kinematic coverage of previously available data in the low to medium Q^2 domain and when combined with the existing world data set allows a calculation of the Nachtmann moments for $n = 2, 4, 6$ and 8 over the Q^2-range $0.2 - 150$ $(\text{GeV/c})^2$. The carbon-to-deuteron ratio of the leading-twist F_2 moments exhibits the well known EMC effect by deviating from the Fermi motion expectation. The deviation is compatible with that observed previously in x space in DIS. For the first time we obtained the carbon-to-deuteron ratio of the total higher-twist contributions to the F_2 moments of the nucleon. Despite large systematic uncertainties, this ratio has a surprising behavior, increasing almost linearly with the moment order n, and lies well below unity for $n < 7$. This suppression of the higher twists in the nucleon bound in the nuclear matter cannot be described by the strong damping of the nucleon excitations in nuclei suggested in Ref. [2]. The comparison between the relative contributions of higher twists in carbon and deuteron suggests a
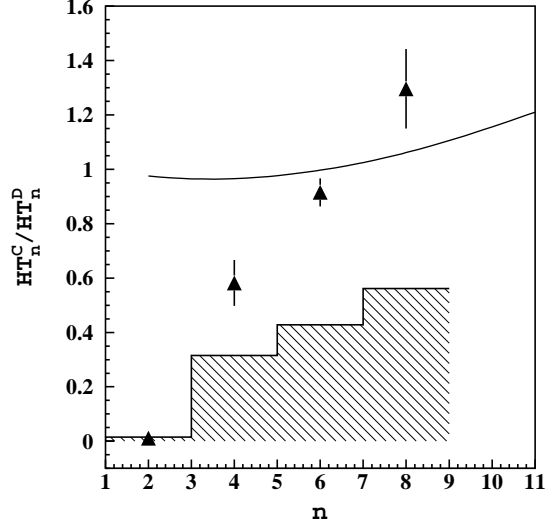
Figure 14: The carbon-to-deuteron ratio of the higher-twists moments at $Q^2 = 2$ $(\mathrm{GeV/c})^2$. The curve is the same as in Fig. 13. The systematic uncertainties are shown by the hatched histogram.
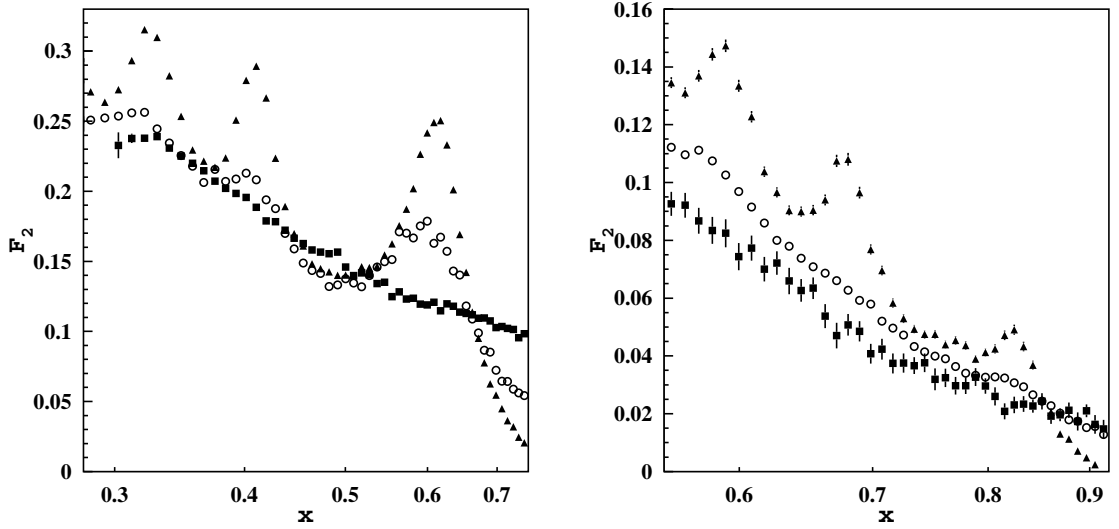
Figure 15: The nucleon structure function F_2 in the resonance region for proton [6] (full triangles), deuteron [7] (open circles) and carbon (full squares) at $Q^2 = 1$ $(\mathrm{GeV/c})^2$ (left) and $Q^2 = 3$ $(\mathrm{GeV/c})^2$ (right). Errors are statistical only.

34
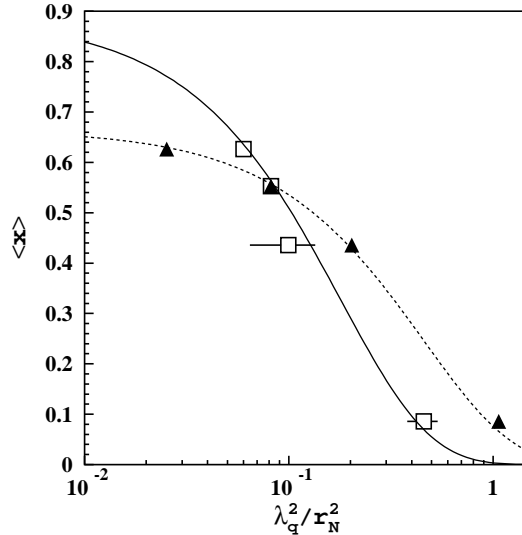
Figure 16: Mean momentum of partons in the nucleon in the deuteron (open squares) and in carbon (full triangles) as a function of their mean free path defined in the text (see Eq. 23). The curves show phenomenological Gaussian parametrizations for the deuteron (solid) and carbon (dashed). Errors are statistical only.

wider distribution of free partons in the bound nucleon. We speculate therefore that the spatial shape of the nucleon, thought as a bag of free partons, is enhanced when it is immersed in the nuclear matter, but in contrast to the rescaling model, the overall probability to find a parton is conserved.

Our analysis indicates a need for further measurements encompassing the kinematic region of Q^2 from 5 to 40 $(\text{GeV/c})^2$ and large x, and $Q^2 > 10$ $(\text{GeV/c})^2$ and low x. The first region can be explored with 12-GeV Jefferson Lab upgrade [73], while the second domain would be accessible with the construction of an electron-ion collider [74].

7. Acknowledgments

References

[1] J.J. Aubert *et al.*, *Phys. Lett.* **B123**, 275 (1983).

[2] M. Anghinolfi *et al.*, *Nucl. Phys.* **A602**, 405 (1996).

[3] R.G. Roberts, *The Structure of the Proton*, Cambridge University Press (1990).

[4] M. Osipenko, hep-ph/0307316 (2003).

[5] M. Arneodo, *Phys. Rept.* **240**, 301 (1994).

[6] M. Osipenko *et al.*, *Phys. Rev.* **D67**, 092001 (2003).

[7] M. Osipenko *et al.*, *Phys. Rev.* **C73**, 045205 (2006).

[8] G. Ricco *et al.*, *Phys. Rev.* **C57**, 356 (1998).

[9] I. Niculescu *et al.*, *Phys. Rev.* **C73**, 045206 (2006).

[10] J. Gomez *et al.*, *Phys. Rev.* **D49**, 4348 (1994).

[11] D.T. Baran *et al.*, *Phys. Rev. Lett.* **61**, 400 (1988).

[12] D.B. Day *et al.*, *Phys. Rev.* **C48**, 1849 (1993).

[13] F.H. Heimlich *et al.*, *Nucl. Phys.* **A231**, 509 (1974).

[14] J. Arrington *et al.*, *Phys. Rev. Lett.* **82**, 2056 (1999).

[15] S.V. Dementii *et al.*, *Yad. Fiz.* **9**, 241 (1969).

[16] J.S. O'Connell *et al.*, *Phys. Rev. Lett.* **53**, 1627 (1984).

[17] P. Barreau *et al.*, *Nucl. Phys.* **A402**, 515 (1983).

[18] R.M. Sealock *et al.*, *Phys. Rev. Lett.* **62**, 1350 (1989).

[19] D.S. Bagdasaryan, YERE-1077-40-88 (1988).

[20] K.C. Stanfield, C.R. Canizares, W.L. Faissler and F.M. Pipkin, *Phys. Rev.* **C3**, 1448 (1971).

[21] J. Arrington *et al.*, *Phys. Rev.* **C53**, 2248 (1996).

[22] R.R. Whitney *et al.*, *Phys. Rev.* **C9**, 2230 (1974).

[23] A.C. Benvenuti *et al.*, *Z. Phys.* **C63**, 29 (1994).

[24] A.C. Benvenuti *et al.*, *Phys. Lett.* **B195**, 91 (1987).

[25] D. Bollini *et al.*, *Phys. Lett.* **B104**, 403 (1981).

[26] M. Arneodo *et al.*, *Nucl. Phys.* **B333**, 1 (1989).

[27] J. Eickmeyer *et al.*, *Phys. Rev. Lett.* **36**, 289 (1976).

[28] J. Bailey *et al.*, *Nucl. Phys.* **B151**, 367 (1979).

[29] S. Hartwig *et al.*, *Z. Phys.* **C2**, 279 (1979).

[30] M.S. Goodman *et al.*, *Phys. Rev. Lett.* **47**, 293 (1981).

[31] M.R. Adams *et al.*, *Z. Phys.* **C67**, 403 (1995).

[32] J. Ashman *et al.*, *Phys. Lett.* **B202**, 603 (1988).

[33] M. Arneodo *et al.*, *Phys. Lett.* **B211**, 493 (1988).

[34] M. Arneodo *et al.*, *Nucl. Phys.* **B333**, 1 (1989).

[35] M. Arneodo *et al.*, *Nucl. Phys.* **B441**, 12 (1995) P. Armadruz *et al.*, *Nucl. Phys.* **B441**, 3 (1995); P. Amaudruz *et al.*, *Z. Phys.* **C53**, 73 (1992); P. Amaudruz *et al.*, *Z. Phys.* **C51**, 387 (1991).

[36] S. Catani *et al.*, *Nucl. Phys.* **B478**, 273 (1996); M. Cacciari and S. Catani, *Nucl. Phys.* **B617**, 253 (2001).

[37] D. Dolgov *et al.* (LHPC and SESAM Collaborations), *Phys. Rev.* **D66**, 034506 (2002); M. Göckeler *et al.* (QCDSF Collaboration), *Phys. Rev.* **D71**, 114511 (2005).

[38] W.L. van Neerven and A. Vogt, *Nucl. Phys.* **B568**, 263 (2000); ibid **B588**, 345 (2000).

[39] S. Simula, *Phys. Lett.* **B493**, 325 (2000).

[40] B.A. Mecking *et al.*, *Nucl. Instr. and Meth.* **A503/3**, 513 (2003).

[41] M. D. Mestayer *et al.*, *Nucl. Instr. and Meth.* **A449**, 81 (2000).

[42] E. S. Smith *et al.*, *Nucl. Instr. and Meth.* **A432**, 265 (1999).

[43] G. Adams *et al.*, *Nucl. Instr. and Meth.* **A465**, 414 (2001).

[44] M. Amarian *et al.*, *Nucl. Instr. and Meth.* **A460**, 460 (2001).

[45] M.E. Christy *et al.*, *Phys. Rev.* **C70**, 015206 (2004).

[46] M. Osipenko, A. Vlassov and M. Taiuti, CLAS-NOTE-2004-020 (2004), http://www.jlab.org/Hall-B/notes/.

[47] P. Bosted, CLAS-Note-2004-005 (2004), http://www.jlab.org/Hall-B/notes/.

[48] C. Ciofi degli Atti, S. Liuti and S. Simula, *Phys. Rev.* **C41**, 2474 (1990); C. Ciofi degli Atti and S. Simula, *Phys. Rev.* **C53**, 1689 (1996).

[49] S. Brodsky *et al.*, *Phys. Rev.* **D4**, 1532 (1971).

[50] H. de Vries *et al.*, *Atomic Data and Nuclear Data Tables* (1986).

[51] L.W. Mo and Y.S. Tsai, *Rev. Mod. Phys.* **41**, 205 (1969); Y.S. Tsai, *Phys. Rev.* **122**, 1898 (1961).

[52] K.S. Egiyan *et al.*, *Phys. Rev.* **C68**, 014313 (2003).

[53] K.S. Egiyan *et al.*, *Phys. Rev. Lett.* **96**, 082501 (2006).

[54] CLAS Physics Database, http://clasweb.jlab.org/physicsdb/.

[55] I. Akushevich *et al.*, *Acta Phys. Polon.* **B28**, 563 (1997).

[56] http://www.physics.unh.edu/maurik/gsim_info.shtml.

[57] Y. Liang *et al.*, *Phys. Rev.* **C73**, 065201 (2006).

[58] O. Nachtmann, *Nucl. Phys.* **B63**, 237 (1973).

[59] http://wwwinfo.cern.ch/asd/cernlib/overview.html.

[60] G. Ricco *et al.*, *Nucl. Phys.* **B555**, 306 (1999).

[61] X. Ji and P. Unrau, *Phys. Rev.* **D52**, 72 (1995); U.K. Yang and A. Bodek, *Phys. Rev. Lett.* **82**, 2467 (1999).

[62] M. Osipenko *et al.*, *AIP Conf. Proc.* **892**, 448 (2007).

[63] MINUIT, CERNLIB WriteUp, http://wwwasdoc.web.cern.ch/wwwasdoc/minuit/minmain.html.

[64] G.B. West, *Phys. Lett.* **B37**, 509 (1971).

[65] R.L. Jaffe, in *Relativistic Dynamics and Quark-Nuclear Physics*, ed. by M.B. Johnson and A. Pickleseimer, Wiley (New York, 1985), pp. 1-82.

[66] A.J. Buras, *Rev. Mod. Phys.* **52**, 199, (1980).

[67] M. Lacombe *et al.*, *Phys. Rev.* **C21**, 861 (1980).

[68] M. Osipenko *et al.*, *Nucl. Phys.* **A766**, 142 (2006).

[69] R. Subedi *et al.*, *Science* **320**, 1476 (2008).

[70] G. Van der Steenhoven, *et al.*, *Phys. Rev. Lett.* **57**, 192 (1986); S. Strauch, *et al.*, *Phys. Rev. Lett.* **91**, 052301 (2003); T.D.Cohen, *et al.*, *Phys. Rev. Lett.* **59**, 1267 (1987); I. Sick, *Nucl. Phys.* **A434**, 677 (1985); R.W.McKeown, *Phys. Rev. Lett.* **56**, 1452 (1986).

[71] F.E. Close, R.L. Jaffe, R.G. Roberts and G.G. Ross, *Phys. Rev.* **D31**, 1004, (1985).

[72] C.E. DeTar and J.F. Donoghue, *Ann. Rev. of Nucl. and Part. Science*, **33**, 235 (1983).

[73] CDR for the Science and Experimental Equipment for the 12 GeV Upgrade (2006); http://www.jlab.org/12GeV/.

[74] Physics Opportunities with e+A Collisions at an Electron Ion Collider - e+A White Paper, EIC Collaboration (2007); http://web.mit.edu/eicc/.